$\mathbf{K_{1-y}Na_yTa_{1-x}Nb_xO_3}$ Thin Films for Integrated Electro-Optics

A dissertation submitted to

ETH ZURICH

for the degree of

Doctor of Natural Sciences

presented by

CHRISTIAN HERZOG

Dipl. Phys. ETH

born 10 September 1975

citizen of Germany

accepted on the recommendation of

Prof. Dr. Peter Günter, examiner
Prof. Dr. Germano Montemezzani, co-examiner

2007

Ich glaube jedem, der die Wahrheit sucht.
Ich glaube keinem, der sie gefunden hat.
–Kurt Tucholsky

To my parents

Contents

Abstract

Potassium tantalate niobate ($KTa_{1-x}Nb_xO_3$, or short KTN) is a perovskite dielectric whose outstanding dielectric and electro-optic properties have attracted a great attention in the optics community in the past decades. Apart from being used as bulk crystals in modulators or deflectors, the prospect of exploiting its large nonlinear-optic coefficients in integrated optic devices has always been appealing. For years, ion implantation has been the only available method to produce waveguides of reasonable quality in this material family, but this approach is inherently restricted by the tunneling losses into the substrate. In the early 1990s, epitaxial growth methods for perovskite oxides yielded initial thin films, but it wasn't until 2004 that the first waveguiding potassium tantalate niobate epitaxial films were reported by the NTT labs in Japan. For the production of good optical quality waveguide devices, the challenge is to find a pair of substrate and thin film materials that share very similar lattice parameters and allow the growth of defect-free thin films with an optically flat surface.

In this thesis we present the first waveguiding thin films of paraelectric potassium sodium tantalate niobate ($K_{1-y}Na_yTa_{1-x}Nb_xO_3$, KNTN) epitaxially grown on potassium tantalate (KT) substrates, the production of ridge waveguides, and electro-optic phase modulation therein. $K_{1-y}Na_yTa_{1-x}Nb_xO_3$ is essentially KTN with a small fraction y of the potassium substituted with sodium, allowing the crystal lattice to be slightly modified to match the KT substrate in the epitaxial growth process, which tremendously improves the crystal quality of the thin film. The work is a continuation of two Ph.D. theses in the Nonlinear Optics Laboratory (Roland Gutmann [1] and Harald Pierhöfer [2]) and marks an important step towards the use of electro-optic KNTN thin films for integrated optic devices.

In the first chapter of this thesis, the basics of dielectric materials, the ferro- and paraelectric phases, and the phase transitions between these phases are introduced. The perovskite and lithium niobate materials and their electro-optic properties are presented. In the second chapter, the fundamentals of guided and integrated thin film optics are discussed and the prominent qualification of KNTN thin films for this field of application is elucidated. Chapters three and four, which have been published in peer-reviewed journals, deal with the details of the production and characterization of planar waveguides and ridge waveguide phase modulation in paraelectric KNTN thin films on KT substrates. More sophisticated devices that could benefit from the particular electro-optic properties of KNTN thin films are discussed in chapter five, before a conclusion of the work presented in this thesis is given in chapter six. Using a cryostatic interferometer setup that was developed for the determination of the electro-optic coefficients of KNTN at low temperatures, the

unclamped Pockels effect of congruent lithium niobate at cryogenic temperatures was investigated and related to the polarization-optic coefficients of this material. This work is presented in Appendix A and was also published in a scientific journal.

Zusammenfassung

Kalium-Tantalat-Niobat ($KTa_{1-x}Nb_xO_3$, kurz KTN) ist ein dielektrisches Material in Perovskitstruktur, dessen außergewöhnliche dielektrische und elektrooptische Eigenschaften in den vergangenen Jahrzehnten große Aufmerksamkeit in der Optik erregt haben. Neben dem Einsatz ganzer Kristalle in Modulatoren und Deflektoren hat die Aussicht auf eine Ausnutzung der großen nichtlinear-optischen Koeffizienten in der integrierten Optik von Anfang an das Interesse an diesem Material geweckt. Für viele Jahre war die Ionenimplantation die einzige verfügbare Methode, um Wellenleiter vernünftiger Qualität in dieser Materialfamilie herzustellen, aber diese Technik ist inhärent durch die Tunnelverluste in das Substrat limitiert. Anfang der 90er Jahre lieferten epitaktische Zuchtmethoden von Perovskitoxiden frühe Muster von Dünnfilmen, aber die ersten wellenleitenden Kalium-Tantalat-Niobat-Filme wurden nicht vor 2004 von den NTT-Labors in Japan veröffentlicht. Für die Herstellung von Wellenleitern guter optischer Qualität besteht die Herausforderung darin, ein Paar von Substrat- und Dünnfilmmaterialien zu finden, die sehr ähnliche Gitterparameter aufweisen und die Zucht defektfreier Dünnfilme mit optisch glatter Oberfläche erlauben.

In dieser Doktorarbeit stellen wir die ersten wellenleitenden Dünnfilme aus paraelektrischem Kalium-Natrium-Tantalat-Niobat ($K_{1-y}Na_yTa_{1-x}Nb_xO_3$, KNTN) vor, die epitaktisch auf Kalium-Tantalat-Substraten (KT) aufgewachsen wurden, sowie die Produktion von Rippenwellenleitern und elektrooptische Phasenmodulation in diesen Wellenleitern. $K_{1-y}Na_yTa_{1-x}Nb_xO_3$ ist im Wesentlichen KTN, wobei ein kleiner Teil y des Kaliums durch Natrium ersetzt wird, was es uns erlaubt, im epitaktischen Zuchtprozess die Gitterabstände an die der KT-Substrate anzupassen, wodurch sich die Kristallqualität der Dünnfilme enorm verbessert. Diese Arbeit baut auf zwei Doktorarbeiten des Nonlinear Optics Laboratory auf (Roland Gutmann [1] and Harald Pierhöfer [2]) und stellt einen wichtigen Schritt auf dem Weg zu integriert-optischen Bausteinen auf der Basis elektrooptischer KNTN-Dünnfilme dar.

Im ersten Kapitel dieser Dissertation werden die Grundlagen dielektrischer Materialien, der ferro- und paraelektrischen Phasen und deren Phasenübergänge eingeführt. Die Materialien der Perovskitfamilie und Lithiumniobat werden vorgestellt, zusammen mit ihren elektrooptischen Eigenschaften. Im zweiten Kapitel werden die Grundsätze der geführten und integrierten Dünnfilmoptik vermittelt, und die ausgezeichnete Eignung von KNTN-Dünnfilmen für diesen Einsatzbereich wird diskutiert. Kapitel drei und vier, die in Fachzeitschriften veröffentlicht wurden, handeln von den Einzelheiten der Herstellung und Charakterisierung von planaren Wellenleitern und der Phasenmodulation in Rippenwellenleitern in paraelektrischen KNTN-Dünnfilmen auf KT-Substraten. Weiter entwickelte Bauteile, die von den außerge-

wöhnlichen elektrooptischen Eigenschaften von KNTN-Dünnfilmen profitieren könn-
ten, werden in Kapitel fünf vorgestellt, worauf in Kapitel sechs ein Fazit der in
dieser Doktorarbeit vorgestellten Forschungsarbeit gezogen wird. Ein kryostatischer
Interferometeraufbau, der für die Messung der elektrooptischen Koeffizienten von
KNTN bei tiefen Temperaturen entwickelt wurde, diente zur Bestimmung des unge-
klemmten Pockelseffekts in kongruentem Lithiumniobat bei kryogenen Tempera-
turen und dessen Beziehung zu den polarisationsoptischen Koeffizienten in diesem
Material. Dieser Teil der Arbeit, der ebenfalls veröffentlicht wurde, wird in An-
hang A vorgestellt.

Chapter 1

Para- and ferroelectric materials and electro-optics therein

This chapter gives a general introduction into the theory of dielectric materials with a special focus on paraelectric and ferroelectric phases, the associated phase transitions and the electro-optic effects in these materials. There are many excellent books on this topic [3, 4, 5, 6] which we can recommend for a more detailed description.

1.1 Dielectrics

A dielectric material is an electrical insulator in solid state, which is to say that upon application of an external electric field, the static *conduction current* flowing through the dielectric material will be extremely small. However, charges within the atoms or molecules of the dielectric material will be redistributed, giving rise to a *displacement current*. The displacement current is of transient nature and ceases to flow once an equilibrium state between the externally applied field and the internal polarization field, created by the displaced charges, is reached. The electrical displacement $\boldsymbol{D}$ can therefore be expressed as

$$\boldsymbol{D} = \varepsilon_0 \boldsymbol{E} + \boldsymbol{P} = \varepsilon_0 \boldsymbol{E} + \varepsilon_0 \chi \boldsymbol{E} = \varepsilon_0 (1 + \chi) \boldsymbol{E} = \varepsilon_0 \varepsilon \boldsymbol{E}, \tag{1.1}$$

where $\varepsilon_0 \approx 8.854 \times 10^{-12}\,\mathrm{F\ m^{-1}}$ is the vacuum permittivity, $\boldsymbol{E}$ is the external electric field, $\boldsymbol{P}$ is the polarization of the material, χ is the susceptibility of the material and ε is the relative permittivity of the dielectric (often called dielectric constant, even though it is not constant in any respect, be it temperature, frequency, material composition...). Hence ε can be understood as the ratio of the amount of electrical energy stored in the dielectric as compared to vacuum. It is important to note that in any anisotropic material ε_{ij} is a tensor of second rank whose number of independent elements depends on the material crystal symmetry.

This much is true for all dielectric materials, but it turns out that we can further differentiate between special types of dielectrics. Many dielectric materials exhibit a behavior that depends on temperature as they exist in different phases which are separated by phase transitions. Phase transitions are structural changes that the material undergoes at specific phase transition temperatures. By far the most

typical case is that of the dielectric passing from a paraelectric high temperature phase to one or several ferroelectric phases at lower temperatures upon crossing the Curie point T_C. One usually talks about paraelectrics or ferroelectrics, meaning that the material is in the respective phase at a given temperature.

1.1.1 Paraelectric phase

In the paraelectric phase, the electric dipoles in the material are macroscopically unaligned in the absence of an external electric field but will be oriented in a preferential direction if such a field is applied to the material. Without the field, paraelectrics exhibit no spontaneous polarization $\boldsymbol{P}_S$, as ferroelectrics do. The paraelectric phase is often isotropic in a (quasi-)cubic crystal symmetry.

1.1.2 Ferroelectric phase

The characteristic feature of the ferroelectric phase is the presence of a macroscopic spontaneous polarization $\boldsymbol{P}_S$ that exists in the absence of an external electric field and whose direction can be reoriented if such a field is applied to the material. The graph of the polarization P as a function of electric field E shows a typical hysteresis behavior as depicted in Fig. 1.1, and in analogy to ferromagnetic materials the term ferroelectrics was coined. As can be seen in the graph, the projection of the high
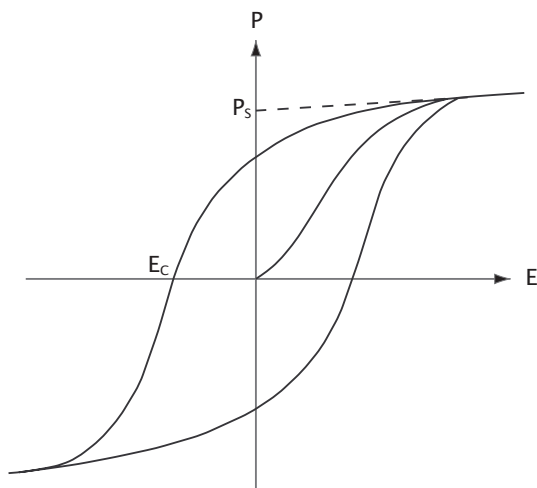
Figure 1.1: Hysteresis behavior of the polarization in ferroelectric materials exposed to an external electric field.

field saturation polarization onto the P axis yields the spontaneous polarization P_S, while the strength of the external field needed to compensate P_S is called the coercive field E_C.

Another typical property of the ferroelectric phase is the formation of domains. Domains are microscopic regions with one specific direction of the spontaneous polarization $\boldsymbol{P}_S$, separated by domain walls. Typical domain dimensions are on the order of μm and neighboring domains tend to be oriented in either an anti-parallel

(180 ° domains) or orthogonal (90 ° domains) way in order to minimize the internal dielectric displacement energy in the material. For practical applications, usually the monodomain state is desired in which all domains are aligned in the same direction. This can be achieved by poling: if the material is subject to an external electric field $E > E_C$, domains will align in the direction of the external field. Since the coercive field E_C often is in the kV/mm range, this direct approach to poling usually is not feasible as breakdown occurs at much lower field strengths. Fortunately, poling is also possible by heating the material above the phase transition temperature into the paraelectric phase, in which the domains disappear. Now a much smaller field is sufficient to align the dipoles and by lowering the temperature into the ferroelectric phase, this configuration can be "frozen" and a monodomain state will result.

Since obviously the existence of $\boldsymbol{P}_S$ creates a preferential direction and breaks the anisotropy of the material, the ferroelectric phase is of lower crystal symmetry. Typical examples are tetragonal $4mm$ or rhombohedral $3m$.

1.1.3 Phase transitions

The individual phases in a dielectric are separated by phase transitions. A phase transition denotes a structural change in the material that alters its crystal symmetry, the dielectric properties and usually a whole set of other parameters. Even though there are typically phase transitions between different ferroelectric crystal structures, by far the most important phase transition in a material is the one between the paraelectric and the ferroelectric phase. In analogy to the ferromagnetic case, the temperature at which this phase change happens is called the Curie point T_C. Closely related to the Curie point T_C is the Curie temperature T_0. We will soon see how.
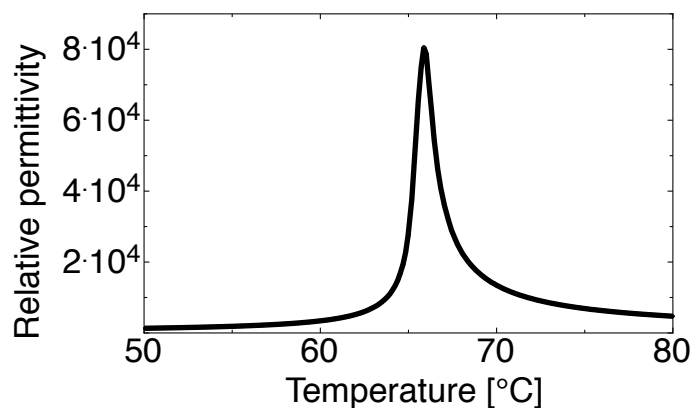

Figure 1.2: Curie-Weiss behavior of the relative dielectric permittivity ε in $\mathrm{Sn_2P_2S_6}$ around the Curie point $T_C \approx 66\,^\circ\mathrm{C}$.

For technical applications, the region around the Curie point is of great importance since the dielectric permittivity ε theoretically diverges at T_0 according to the

famous Curie-Weiss law

$$\varepsilon(T) = \frac{C}{T - T_0}, \quad T > T_0 \tag{1.2}$$

and in practice usually shows an enormous continuous peak. C in the above formula is the material-specific Curie constant. Since the electro-optic and nonlinear-optic coefficients are related to ε (see section 1.4), devices exploiting these coefficients can benefit from a performance boost if operated close to T_0. Fig. 1.2 shows, as an example, the divergence of the relative permittivity in $Sn_2P_2S_6$ at $f = 1$ kHz around the phase transition at $T_C \approx 66\,°C$.

Depending on the behavior of P_S at the Curie temperature T_0, the phase transition can be of either first or second order. As can be seen in Fig. 1.3, in a first-order phase transition P_S drops discontinuously from a nonzero value to zero at T_0, while a second-order transition is characterized by a smooth decrease.
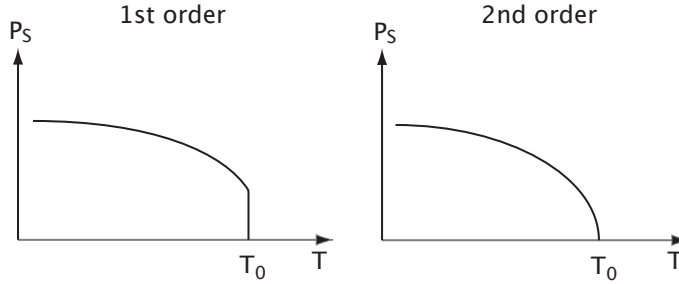
Figure 1.3: Behavior of the spontaneous polarization P_S at the phase transition temperature for a phase transition of first and second order.

In a transition of first order, the two phases coexist at T_0 and the Curie temperature is related to the Curie point by $T_C > T_0$. Conversely, a material undergoing a second-order transition always is in either one of the two phases and $T_C = T_0$. We will not cover the complete theory of ferroelectrics here and instead just give a phenomenological idea about the source of the two types of phase transitions. The complete derivation can be found in any ferroelectrics book [3,4,5,6] and is based on the calculations performed by Müller, Ginzburg and Devonshire. The theory starts by expanding the Gibbs free energy G of the system into a Taylor series in powers of the spatial polarization components P_i:

$$G = G_0 + \sum_{n=1} R_n(P_x^{2n} + P_y^{2n} + P_z^{2n}), \tag{1.3}$$

where G_0 is the free energy in the paraelectric phase and R_n are Taylor coefficients. Energy minimization then requires

$$\left(\frac{\partial G}{\partial P_i}\right)_{P_S} = 0, \tag{1.4}$$

which yields a set of equations for P_S that can be plotted as shown in Fig. 1.4.
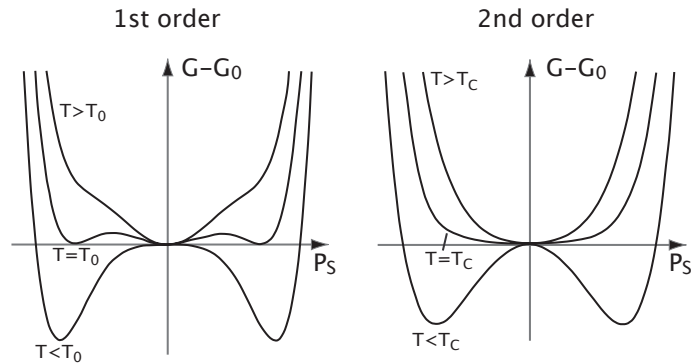
Figure 1.4: Gibbs free energy as a function of the spontaneous polarization for a phase transition of first and second order.

The aforementioned properties of the two types of phase transitions can be understood from this graph: the coexistence of both phases (paraelectric with $P_S = 0$ and ferroelectric with $P_S > 0$) around the Curie temperature for a transition of first order. This leads to the discontinuous drop in P_S and also explains superheating and -cooling at $T > T_0$ and $T < T_0$, respectively. On the other hand, a second-order transition does not allow metastable polarization states and the condition of the system is always well defined.

1.1.4 Classification of ferroelectrics

Since the ferroelectric family of materials is so huge and diverse, various systems of classification have been proposed in the past. We single out the two that have a direct relation to the materials covered in this thesis.

Relaxors

The Curie-Weiss law introduced in Section 1.1.3 is valid only for what are called *normal* ferroelectrics. Apart from these, there's a group of ferroelectrics called the *relaxors* which exhibit a broader peak in ε that can be described by

$$\frac{1}{\varepsilon(T)} - \frac{1}{\varepsilon_{\max}} = C'(T - T_{\varepsilon_{\max}})^n, \quad T > T_0 \text{ and } 1 < n < 2. \tag{1.5}$$

Materials of this class pass through a diffuse phase transition which is caused by local inhomogeneous composition variations and we will see later that many perovskite solid solutions belong to the relaxor-type group of ferroelectrics. The dielectric behavior of relaxors shows two characteristic features: with increasing frequency, the maximum of their dielectric peak decreases in value and is shifted to higher temperatures (see Fig. 1.5). This decrease has to be taken into account for high-frequency applications. For KTN, the undoped parent material of the KNTN used in Chapters 3 and 4, the relative permittivity up to 3 GHz has been measured by Itoh et al. [7]. According to this classification, our KNTN thin films should therefore exhibit a dielectric behavior which can be described by equation 1.5, but
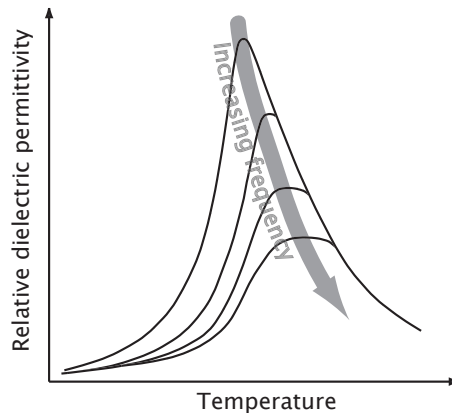
Figure 1.5: Dielectric behavior of relaxor ferroelectrics. The dielectric maximum decreases and shifts to higher temperatures with increasing frequency.

the measurements performed in Chapters 3 and 4 could frequently be approximated better by equation 1.2. As is often the case for dielectrics, KNTN seems to be an intermediate material that defies a clear classification into distinct categories.

Displacive and order/disorder dielectrics

In older literature on ferroelectrics, a great deal of importance is usually attributed to the distinction between *displacive* and *order/disorder* ferroelectrics. In displacive materials, induced dipoles generate a net polarization in the ferroelectric phase, while the paraelectric phase in the absence of dipoles is microscopically nonpolar. The Curie constant is usually around 10^5 K. Conversely, order/disorder dielectrics possess permanent dipoles which exist in two equally populated equilibrium positions in the paraelectric phase and make the material nonpolar only in a macroscopic average. The Curie constant is significantly lower in these materials, typically in the 10^3 K range.

In the past thirty years, many measurements have been performed however that are incommensurate with this sharp discrimination [8], as only very few materials show a textbook behavior of either type, while most exhibit a mixture of the two. Today the concept of these two distinct groups of ferroelectrics is considered obsolete and unified theories with more than one order parameter have been suggested [9].

After this detour into ferroelectrics theory, we will now concentrate on the dielectric behavior of the two materials that have been investigated in the course of this thesis: $K_{1-y}Na_yTa_{1-x}Nb_xO_3$ and lithium niobate.

1.2 The $K_{1-y}Na_yTa_{1-x}Nb_xO_3$ family

The potassium sodium tantalate niobate ($K_{1-y}Na_yTa_{1-x}Nb_xO_3$, from now on we will also use KNTN) family is a classic example of a perovskite solid solution [10], which is to say a blend of the two materials potassium tantalate ($KTaO_3$, KT) and

potassium niobate ($KNbO_3$, KN), with a small fraction of the potassium replaced by sodium. Before going into the KNTN material family in detail, we have to introduce the technologically important group of perovskite dielectrics.

1.2.1 Perovskites

The perovskite group of dielectrics was termed after the mineral $CaTiO_3$ by the same name. The general formula for perovskites is ABX_3, but only the perovskite oxides ABO_3 show ferroelectricity. The common crystal structure of all perovskite oxides is shown in Fig. 1.6 and can be regarded as either a collection of BO_6 octa-
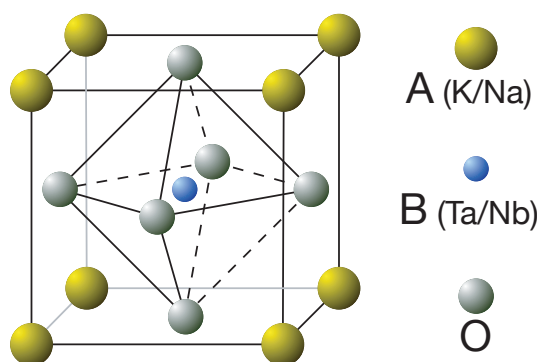
Figure 1.6: The perovskite crystal structure ABO_3.

hedra with the A atoms occupying the spaces between or a cubic close packing of A and O ions with the B ions at the interstitial positions. The dielectric properties of perovskites can be described by the rigid oxygen octahedra that stay largely undeformed by external electric fields and the "rattling" of the B ions inside the octahedra. The temperature dependence of the dielectric properties of perovskites is characterized by the Curie transition from the cubic paraelectric to one or more subsequent ferroelectric phases when the temperature of the system is decreased. T_C spans a wide range of temperatures across different perovskites, from a few K (e.g. in KT) to more than 1500 K in $CaTiO_3$. In the ferroelectric phase(s), the cubic unit cell shown in Fig. 1.6 gets slightly deformed which is responsible for the formation of P_S.

1.2.2 $KTaO_3$

Potassium tantalate is one of the constituents of the KNTN solid solution. It is paraelectric above a second-order phase transition at $T_C \approx 4$ K [11] and with $KNbO_3$ shares almost equal lattice parameters, a high refractive index around 2.2, a wide transparency range from 365 nm to 4 μm, and high electro-optic coefficients. Its dielectric properties follow the Curie-Weiss law down to approximately 50 K below which quantum effects start to play a role [12]. The growth of KT has been described in detail in Gutmann's Ph.D. thesis [1].

1.2.3 KNbO$_3$

As already mentioned, the paraelectric phase of KN is structurally very similar to KT, but the Curie point lies much higher, at $T_C \approx 711$ K. At this temperature, the crystal structure changes from cubic $m3m$ to tetragonal $4mm$. At 501 K, a second phase transition modifies the crystal symmetry to orthorhombic $mm2$ and at 243 K, a rhombohedral phase with symmetry $3m$ appears. All phase transitions are of first order. The relative permittivity reaches values of more than 10^4 around the Curie point [13] which makes the material interesting for electro- and nonlinear-optics applications. The spontaneous polarization at room temperature amounts to $P_S = 41$ μC/cm^2. Both KT and KN are usually grown in the top-seeded solution growth (TSSG) method [14].

1.2.4 KTa$_{1-x}$Nb$_x$O$_3$

The structural similarity of KT and KN allows for the growth of crystals of the solid solution potassium tantalate niobate KTN. In such a composite material, the B sites in the ABO$_3$ perovskite structure are partly occupied by tantalum and partly by niobium atoms. Since the tiniest variations in the growth parameters (and probably even statistical fluctuations) will influence the incorporation of either element into the octahedra, it is obvious that the Ta/Nb ratio will not be completely uniform across the whole crystal. It is this local inhomogeneity that is responsible for the relaxor-type phase transition in KTN.

The single most appealing feature of KTN is the fact that by varying the Nb/Ta ratio x, the Curie point T_C can be shifted almost linearly between 4 K ($x = 0$, pure KT) and 711 K ($x = 1$, KN). Fig. 1.7 illustrates this tunability in the KTN phase diagram.
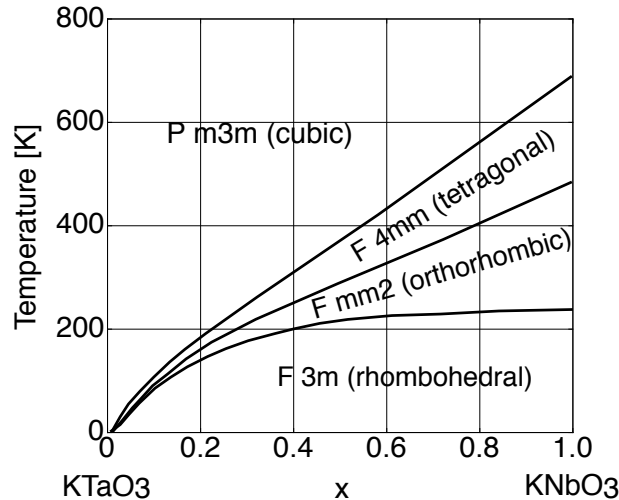
Figure 1.7: Phase diagram of the The KTa$_{1-x}$Nb$_x$O$_3$ solid solution system. P and F indicate the paraelectric and ferroelectric phases, respectively.

It is this truly unique asset of KTN that makes this material so interesting for

electro-optic applications [15, 16] since the dielectric [17], electro-optic or nonlinear-optic properties can be tailored to any given operating temperature.

1.2.5 $K_{1-y}Na_yTa_{1-x}Nb_xO_3$

KNTN as a material is not much different from KTN since the Na fraction y is usually kept very small (a few percent) and the sodium acts like a dopant. It does change one very important property though: it allows the lattice parameters of an epitaxially grown KNTN thin film to be adjusted to the KT substrate it is grown on, thereby reducing internal stress in the film. This method that tremendously increases the crystal quality of such thin films was developed by Pierhöfer [2] and has been perfected since. In the next chapters we will see that by incorporating $2-5$ % of sodium into the KTN material, electro-optic thin films of optical quality could be grown and structured into a phase modulator.

1.3   Lithium niobate

Lithium niobate (LN), whose low-temperature electro-optic properties have been determined in Appendix A, is a very important material in the telecommunications and related industries as it possesses large pyroelectric [18, 19, 20], piezoelectric, electro-optic, photoelastic, acousto-optic, photovoltaic and photorefractive coefficients. A very exhaustive review article detailing every aspect of lithium niobate research has been published by Weis and Gaylord [21], and its properties are also compiled in a book [22]. LN is no perovskite but exhibits a more complicated oxygen octahedra structure, shown in Fig. 1.8. The niobium atoms again sit inside the octahedra, but now the cation order is Nb, vacancy, Li, Nb, vacancy, Li...

Figure 1.8: Crystal structure of lithium niobate.

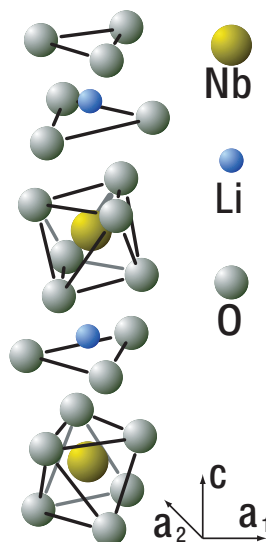LN shows one phase transition of second order from the paraelectric to the ferro-electric phase of trigonal $3m$ symmetry. The Curie point $T_C = 1486$ K is one of the highest of all ferroelectrics, and since it lies only ≈ 50 K below the melting point, the paraelectric phase of LN is neither well examined nor technologically relevant. When grown in the Czochralski method, stoichiometry allows compositions from about 45 to more than 49 mol% Li_2O [23], but the highest quality is achieved for the congruent composition of 48.38 mol% Li_2O [24].

1.4 Electro-optics

The term electro-optics describes the change of the refractive index of a material caused by an electric field applied to the material. Again we will only give a phenomenological description of the associated effects and refer to literature [25] for the complete theory. The change in refractive index in powers of the external field can be described in Einstein and tensor notation by the deformation of the optical indicatrix:

$$\Delta \left(\frac{1}{n^2} \right)_{ij} = r_{ijk} E_k + R_{ijkl} E_k E_l, \tag{1.6}$$

where r_{ijk} are the linear (Pockels) and R_{ijkl} are the quadratic (Kerr) electro-optic coefficients. An equivalent description can be given via the linear and quadratic polarization-optic coefficients f_{ijk} and g_{ijkl}:

$$\Delta \left(\frac{1}{n^2} \right)_{ij} = f_{ijk} P_k + g_{ijkl} P_k P_l, \tag{1.7}$$

where P_i is the field-induced polarization in direction i. Of practical interest is usually the refractive index change Δn_x induced by an electric field E_j in one specific crystal direction x, which can be deduced in contracted tensor notation from equation (1.6) by exploiting the crystal symmetry and the fact that typically $\Delta n \ll n$ (no Einstein summation here, $x = 1, 2$ or 3):

$$\Delta n_x \approx -\frac{n_x^3}{2} \left(r_{xj} E_j + R_{xj} E_j^2 \right). \tag{1.8}$$

In an attempt to reduce the temperature- and frequency-dependence of the linear and quadratic electro-optic coefficients, they can be expressed as a function of the dielectric permittivity and the linear and quadratic polarization-optic coefficients:

$$r_{ijk} = f_{ijm} \varepsilon_0 (\varepsilon_{mk} - 1) \quad \text{and} \tag{1.9}$$

$$R_{ijkl} = g_{ijmn} \varepsilon_0^2 (\varepsilon_{mk} - 1)(\varepsilon_{nl} - 1). \tag{1.10}$$

Depending on the crystal symmetry, also f_{ijk} and g_{ijkl} can be related [26], but as f_{ijk} are a function of both g_{ijkl} and P_S, only the quadratic polarization-optic coefficients are largely temperature-independent and don't differ much for various types of perovskites [27] (see Appendix A for an example).

The linear Pockels coefficients only exist in non-centrosymmetric materials since an asymmetric anharmonic potential is required for even powers in the Fourier series of the polarization [28], and since these materials are also piezoelectric, a differentiation into the clamped coefficients r_{ijk}^S and the free (unclamped) values r_{ijk}^T is necessary. The clamped effect is measured in a rigidly mounted crystal or at high frequencies, while the free coefficients also include a contribution from the converse piezoelectric effect [21].

In Chapters 4, 5 and in Appendix A we will talk about devices utilizing the electro-optic effect, but first let's have a look at the electro-optic properties of the materials we have introduced in this chapter.

1.4.1 $\mathbf{K_{1-y}Na_yTa_{1-x}Nb_xO_3}$

Due to the centrosymmetric nature of the paraelectric phase in KNTN, just the ferroelectric phase exhibits the Pockels effect. Above T_C, only the quadratic electro-optic effect can be used. Since the relative permittivity reaches extremely high values in KNTN (see [29]), we can also expect huge quadratic (in both phases) and linear (below T_C) coefficients according to equation (1.9). Indeed, the linear electro-optic coefficients of the KTN (up to 1400 pm/V) family rank among the highest of all inorganic ferroelectrics [30], and in the paraelectric phase, the largest Kerr coefficient ($5 \cdot 10^{-15}$ m^2/V^2) ever reported was measured [13].

1.4.2 Lithium niobate

Since the phase transition temperature of LN is so high, its electro-optic coefficients at room temperature [21] are rather small compared to KNTN, yet the material has become the standard ferroelectric in commercial telecommunications devices. $r_{333}^T \approx 32$ pm/V, the highest coefficient at room temperature and HeNe wavelength, is outperformed by several orders of magnitude by KTN with a phase transition close to the operating temperature [30]. The behavior of r_{333}^T at cryogenic temperatures has been measured in the course of this thesis. This work is described in Appendix A.

Chapter 2

Thin film optics

This chapter motivates the transition from traditional free-space to state-of-the-art integrated guided optics and gives a general introduction to thin film optic design, fabrication and KNTN waveguides.

2.1 Free-space optics

In the earlier days of electro-optics, experiments were mainly set up in a free-space configuration with bulk crystals (for an example of electro-optic modulation and beam deflection in KTN, see [31]). A typical setup is depicted in Fig. 2.1 which shows the cryostat electro-optic system described in Chapter 4. Such an assembly

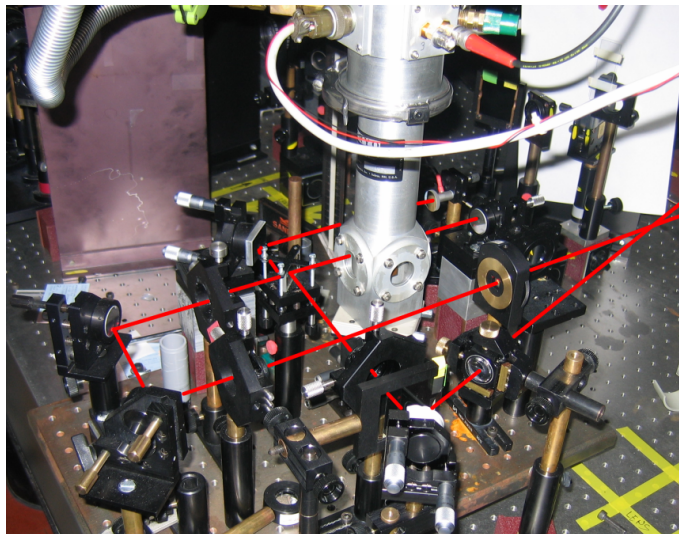Figure 2.1: Typical free-space electro-optical setup with bulk crystals.

is usually built up fast and provides a lot of experimental flexibility, but there's a whole list of drawbacks that became apparent as technology evolved. Apart from taking a lot of space on the optical table, some of the main issues are (as far as electro-optic modulator setups are concerned):

- miniaturization of devices is very difficult

- interaction length is limited by the size of the crystal and the diffraction of the beam

- externally applied electric fields are small due to large electrode spacing

- power density is limited by the laser which might prevent efficient nonlinear-optic effects

- high overlap between external electric field and light field is difficult to achieve

- reliable alignment and long-term stability are big challenges

Hence, there's a strong motivation to devise a technology that allows to overcome as many of these shortcomings as possible.

2.2   Guided optics

The solution is to find a way to confine the light intensity in 1-D (slab waveguide), 2-D (ridge waveguide) or even 3-D (quantum dot) and henceforth take advantage of so-called *guided optics*. The confinement can be achieved by either forcing the light to propagate in a region with an elevated index of refraction (see Fig. 2.2) or by impeding light propagation outside the selected region by a photonic bandgap structure ([32], Fig. 2.3 shows an example).   In the last few decades, waveguides
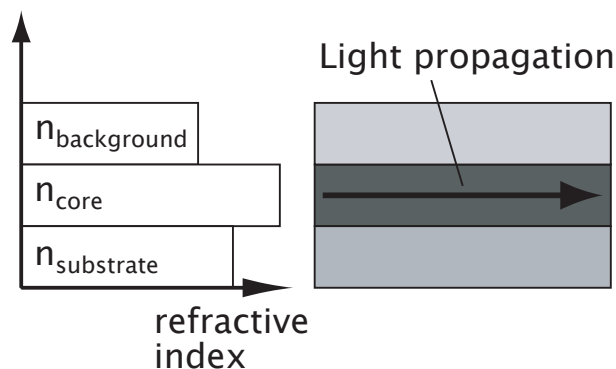
Figure 2.2: Confining light propagation to core area by elevated refractive index. Typically $n_{core} > n_{substrate} > n_{background}$.

have been demonstrated in almost any conceivable material: dielectrics, semiconductors, metals (then called plasmons [34]), organic materials [35], gases [36], and liquids [37]. By taking advantage of the tremendous advance in (sub)micron lithography and etching processing for the fabrication of the waveguides, most of the problems addressed in the list in the previous section can be tackled quite readily:

- miniaturization: micrometer dimensions are standard, nm sizes not uncommon for plasmonic waveguides

- interaction length: can be hundreds of km in doped fibers (EDFAs, [38])
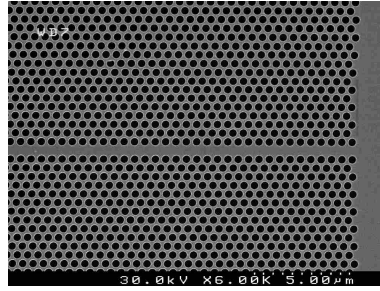
Figure 2.3: Line defect waveguide in photonic bandgap structure, from [33]. Light propagation is only possible in the horizontal waveguide region.

- external fields strength: also electrodes can be μm apart, the field strength therefore is high

- power density: the optical power is confined to a few μm^2 or less, extreme energy densities can be achieved even with low-power lasers

- field overlap: waveguides and electrodes can be placed very close to each other to maximize the overlap between the optical mode and the modulation field

- alignment: fiber coupling with V-grooves is a standard technology [39]

It is obvious that guided optics offers an overwhelming set of benefits over traditional free-space optics, and not surprisingly it has almost completely superseded the latter except in very special fields of application [40].

2.3 Thin film optics

2.3.1 Fabrication

The term *thin film optics* describes the production of optical elements in a thin waveguiding layer of a certain material. The waveguide layer can be created by either inducing a local *index barrier* in the material at a certain depth (for example by ion implantation [41]), or by creating an *index step* when said layer is mounted on top of another material with a lower refractive index. To this end, methods as diverse as bonding split-off films of lithium niobate [42, 43], spin coating thin polymer films [44] or growing a high index film of one material onto another with lower index by metalorganic chemical vapor deposition (MOCVD), molecular beam epitaxy (MBE), plasma sputtering, pulsed laser deposition, or liquid phase epitaxy (LPE) have been used in the past. Once the film is in place, vertical confinement of the light is obtained by the refractive index contrast between the waveguiding core layer and the surrounding substrate and background materials. For the horizontal confinement, the waveguiding layer is usually structured by transferring ridge or channel waveguide designs from a lithographically patterned photoresist into the target material by some sort of etching like reactive ion etching (RIE), plasma etching, (anisotropic) wet etching or sputter etching. The waveguiding material might

be a passive dielectric or exhibit electro-optic or nonlinear-optic activity if tunability, modulation, second-harmonic generation (SHG) or similar effects are desired. We will have a look at some applications of guided thin film optics in Chapter 5. While a huge variety of materials and processing procedures has been described in literature [45, 46, 47, 48, 49, 50, 51], we will concentrate on the narrower topic of guided optics in epitaxial thin films of para- and ferroelectrics for the remainder of this chapter.

2.3.2 Design

The design of a thin film optics device can be a complex task and usually necessitates the deployment of several specialized software packages like mode solvers [52] and finite-element field simulators [53]. The *optical part* of the design work usually evolves around the following criteria:

- typically monomodal propagation for just one (polarization-maintaining) or both (TE and TM, polarization-insensitive) polarizations

- low propagation losses, determined mainly by the scattering of the guided intensity at the surface and sidewalls of the waveguide

- low bending losses for non-straight waveguides

- low insertion losses for the input and output couplers, which can sometimes be improved by tapering the waveguide

For electrically driven active devices, the *electrode design* typically includes the following tasks:

- maximize efficiency and frequency response of the electrode pattern. For HF applications, usually impedance-matched traveling wave electrodes are necessary

- optimize overlap between guided light and external modulation field, taking into account the sometimes unfavorable dielectric permittivity distribution (see Chapter 4 for an example)

- allow good contacting and reliable packaging

Once the waveguide structures have been produced, the electrodes (usually consisting of one or several layers of metal) are typically deposited on the surface by some sputtering process. For vertical field configurations, also buried metallic or transparent (indium tin oxide, ITO) electrodes might be used.

2.4 $K_{1-y}Na_yTa_{1-x}Nb_xO_3$ thin film optics

In Chapter 1, the KTN material family has been introduced. Due to its outstanding electro-optical properties and the well-investigated excellent optical quality of the bulk material, there's a strong motivation to exploit these assets in integrated optics

devices. First steps in this direction have been taken in our group by Gutmann [1] and later Pierhöfer [2], and recently a group of NTT labs [54] has demonstrated buried KTN waveguide devices. In the course of this Ph.D. thesis, we first demonstrated slab waveguiding in planar KNTN thin films on KT substrates and then built a ridge waveguide phase modulator. We will now generally introduce the KNTN thin film complex before talking about planar waveguiding in Chapter 3, the modulator in Chapter 4 and some possible future applications in Chapter 5.

KNTN thin films grown by liquid phase epitaxy (LPE) on KT substrates and then structured into electro-optic devices are almost ideal candidates for high-performance applications for several reasons:

- prospect of low-loss waveguides

- extremely high linear or quadratic electro-optic coefficients with a tunable phase transition temperature

- wide transparency range

- robust and very stable material

- flexible electrode design with conducting KT substrates

We will now walk through these points individually.

2.4.1 Low losses

In step-index waveguides (in contrast to the index barrier waveguides mentioned earlier which also exhibit tunneling losses), the dominant loss mechanism is the scattering of the guided light at the waveguide interfaces. The propagation losses as a function of the wavelength λ, the root mean square interface roughness σ_{RMS} and the refractive index contrast Δn between the waveguide material and the adjacent medium are given by [42]

$$\alpha_{\mathrm{scat}} \propto \frac{\sigma_{\mathrm{RMS}}^2 (\Delta n)^2}{\lambda^{\gamma}} \tag{2.1}$$

where $\gamma = 4$ is only valid under the assumption of perfect Rayleigh scattering [55]. However, recent results [56] suggest that $2 < \lambda < 4$, depending on the waveguide dimensions and the correlation length of the scattering centers. Hence, for a given wavelength we should have smooth interfaces and a low index contrast in order to minimize scattering losses. The first requirement is actually three-fold: we have the KT-KNTN interface, the as-grown horizontal top of the waveguide and the etched side walls, the last two of which are KNTN-air interfaces.

The quality of the KT-KNTN interface is determined by the flatness of the polished KT substrates - a surface roughness of $\sigma_{\mathrm{RMS}} < 2$ nm is readily achievable and since the KNTN grows onto this interface epitaxially, this interface is of practically no concern. The other two interfaces are more important: Pierhöfer has shown [2] that by matching the crystal lattice of the KNTN to the KT substrate with the right amount of sodium dopant, a very flat thin film surface is obtainable. Indeed we have
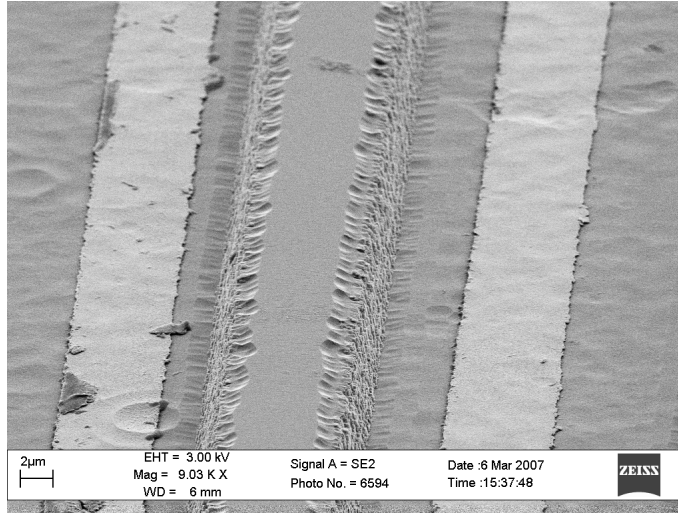
Figure 2.4: Scanning electrode microscopy (SEM) image of a KNTN waveguide with side electrodes.

reported an as-grown roughness of $\sigma_{\mathrm{RMS}} = 21$ nm in Chapter 3. Fig. 2.4 shows a scanning electron microscopy (SEM) picture of a KNTN ridge waveguide. The good optical quality of the top surface is obvious compared to the third kind of interface: the etched sidewalls. For these, a surface roughness of $\sigma_{\mathrm{RMS}} = 55$ nm has been measured by atomic force microscopy (AFM). It is therefore clear that propagation losses are presently limited by the etching process and the value of about 8 dB/cm (Chapter 4) can be significantly reduced with an optimized etching step. The second requirement - a low index contrast - gives us fewer degrees of freedom. For the KT-KNTN interface, the contrast is given by the material indices anyway, and in fact a higher contrast would be favorable to achieve a better vertical confinement of the mode. At the KNTN-air interfaces, the index contrast is huge ($\Delta n \approx 1.2$) which confirms that the etched sidewalls are by far the dominant sources of losses. Coating the waveguide with an intermediate-index material like SiO_2 or Si_3N_4 has therefore been proposed to further decrease the losses (see Chapter 4).

2.4.2 High electro-optic coefficients

As we have seen in Section 1.4, KNTN possesses almost unrivaled electro-optic coefficients in both the paraelectric as well as the ferroelectric phase if the phase transition tunability is exploited and T_C is tailored to be close to the operating temperature. When devising an electro-optic device based on KNTN thin films, one of the first design decisions concerns the phase the material is to be operated in. Both phases have their specific pros and cons that are summarized in table 2.1 and now will be described in detail:

① and ⑤: while for the Pockels effect in the ferroelectric phase the refractive index change Δn is a linear function of the applied electric field strength E, Δn depends quadratically on E for the Kerr effect in the paraelectric phase (see Section

Table 2.1: Advantages and disadvantages of ferro- and paraelectric KNTN thin films

	Pros	Cons
Ferroelectric	① High unbiased coefficients	② Huge discrepancy between bulk and thin film values ③ Domains that require poling
Paraelectric	④ Isotropic, no domains → polarization-insensitive devices ⑥ 40 % of bulk coefficient in thin film	⑤ High DC bias needed for low modulation amplitude

1.4). This implies that by biasing the paraelectric material with a DC voltage, the effective AC amplitude required to obtain a certain Δn can be reduced. Indeed an equivalent Pockels coefficient of 600 pm/V has been measured in paraelectric KTN by Fujiura [13] for a bias of 62 V/mm. Note however that the addition of high DC voltages to a high frequency AC signal is technologically tricky and thus the unbiased operation in the ferroelectric phase is favorable.

②, ③ and ⑥: as we have already seen in Chapter 1, the formation of domains in the ferroelectric phase is necessary to minimize the internal energy of the material. This constraint has so far prevented epitaxial thin films from being macroscopically and permanently poled into a monodomain state [57, 58]. Consequently, the effective electro-optic coefficient in multidomain ferroelectric thin films is at least one order of magnitude lower than the value in a single-domain bulk crystal [59, 60]. Conversely, we have demonstrated a quadratic thin film electro-optic coefficient in the paraelectric phase that reaches 40 % of the bulk value (see Chapter 4).

④: in contrast to the multidomain ferroelectric phase in which domains oriented in different directions affect the polarization state of the propagating light and domain walls give rise to scattering losses, we face a homogeneous and isotropic material in the paraelectric phase. This is important especially for the phase modulator presented in Chapter 4 since the TE and TM polarizations have to propagate independently and without changing their state.

A careful consideration of the above reasons led us to the conclusion to work with paraelectric KNTN thin films.

2.4.3 Wide transparency range

We have seen in Chapter 1 that the KTN family is transparent from 365 nm to 4 μm. Even though the topic of this thesis is the investigation of electro-optic modulators that operate mainly in the infrared telecom wavelength region, the KNTN thin films presented here could also be interesting for applications like second-harmonic generation in waveguides [61, 62] which would benefit from the wide transparency range.

2.4.4 Flexible electrode design

For electro-optic devices that require an electric field to be applied to the material in the vicinity of the optical mode, two basic electrode configurations are possible as depicted in Fig. 2.5: (A) standard lateral electrodes (see Fig. 2.4 for an example) or (B) a vertical field distribution. The side electrodes are rather easy to produce using
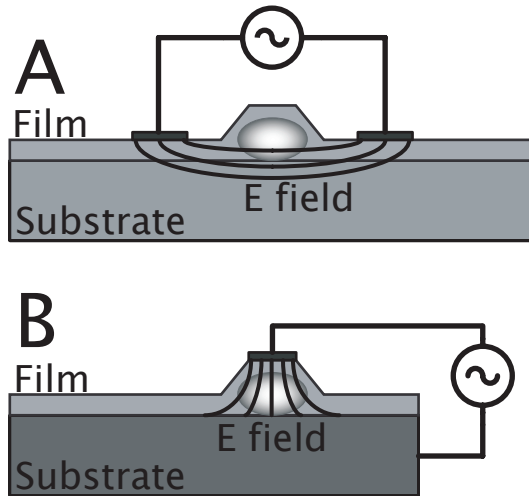

Figure 2.5: Two possible electrode configurations for electro-optics in KNTN thin films.

standard lift-off photolithography and metal deposition, but as will be discussed in Chapter 4, a sufficient overlap of the generated field and the optical mode is not always readily achieved. Top and bottom electrodes have the prospect to deliver the modulation field more directly to the optical mode, but their fabrication is a lot less straightforward.

The top electrode can be deposited onto the waveguide by photolithography and sputter deposition, but standard electrode materials like Cr and Au cannot be used since metallic electrodes would create losses of unacceptable proportions. Instead, a transparent electrode material like indium tin oxide (ITO) has to be used whose electrical properties render high performance devices more difficult.

For the bottom electrode, work has been started [2] to dope the KT substrates with barium which increases their conductivity sufficiently to make them usable as electrodes. Other schemes like buried metal or ITO electrodes [42] are not possible in our case since these electrodes would not survive the LPE growth at temperatures higher than 850 °C.

The decision for either one of the two electrode configurations has to be based on a multitude of factors like waveguide dimensions, mode polarization, material orientation and desired electro-optic coefficient, processing compatibility and the performance target of the device.

We would also like to point out the fact that Ansermet's claim [63] of a $d \approx 15$ μm thin surface layer in KTN with completely altered dielectric properties could not be

confirmed and may be the result of imperfect sample preparation in [63].

Now that we have the required materials and knowledge, we will talk about devices and their fabrication in the following three chapters.

Chapter 3

Epitaxial K$_{1-y}$Na$_y$Ta$_{0.66}$Nb$_{0.34}$O$_3$ thin films for optical waveguiding applications [†]

Monomodal slab waveguides in lattice-matched epitaxial thin films of paraelectric potassium sodium tantalate niobate K$_{1-y}$Na$_y$Ta$_{0.66}$Nb$_{0.34}$O$_3$ (KNTN, $y \approx 0.02$) on paraelectric potassium tantalate KTaO$_3$ (KT) substrates without surface polishing have been fabricated for the first time. A surface roughness of 21 nm (RMS) has been measured by atomic force microscopy (AFM). The film thickness, $d = 1.4$ μm, and refractive index contrast, $\Delta n = 8 \times 10^{-3}$, have been deduced from the intensity profile of the guided mode at $\lambda = 633$ nm.

3.1 Introduction

Devices based on electro-optic (EO) thin film waveguides are promising candidates to achieve smaller, faster and cheaper optical switches and modulators. Structures as diverse as lithium niobate smart-cut films [64], EO polymers [65], α particle implanted KLiTaO$_3$ [66] waveguides or silicon-on-insulator (SOI) microring resonators [67] are under investigation to this end. One of the most auspicious methods is the liquid-phase epitaxial growth of para- or ferroelectric thin films on lattice-matched substrates, due to the huge electro-optic coefficients commonly found in this material family and the prospect of a good optical quality of both the substrate-film interface and the thin film surface. Recent results in this field include the growth of KTa$_x$Nb$_{1-x}$O$_3$ (KTN) thin films on MgAl$_2$O$_4$ substrates [68] and a low driving voltage EO modulator with buried KTN waveguides [69]. In order to achieve low optical losses, an excellent matching of the lattice parameters at the substrate-thin film interface and a small surface roughness of the film are of paramount importance. In this paper we present for the first time monomodal slab waveguiding in potassium sodium tantalate niobate K$_{1-y}$Na$_y$Ta$_{0.66}$Nb$_{0.34}$O$_3$ (KNTN, $y \approx 0.02$) thin films epitaxially grown on potassium tantalate (KT) substrates with an as-grown optically flat surface, thereby eliminating the need for surface polishing. The quality of the

---

[†]This chapter has been published in JOSA B [29].

lattice-matching and the film surface are confirmed by X-ray diffraction (XRD) measurements and atomic force microscopy (AFM) scans, respectively. By measuring the light intensity profile of the guided mode and inverting the Helmholtz equation of a guided slab waveguide mode, the refractive index contrast Δn between the substrate and thin film material, as well as film thickness d, are derived (refined method from [70, 71]). Refractive index and permittivity parameters of the thin film are compared to the bulk values measured by the femtosecond time delay and interdigital electrode impedance method, respectively.

3.2 Potassium sodium tantalate niobate thin film growth, waveguide preparation and material characterization

### 3.2.1 The $K_{1-y}Na_yTa_{1-x}Nb_xO_3$ material family

The growth of KNTN thin films on KT substrates is interesting for the following reasons: for optical purposes, it is possible to lattice-match the epitaxial film to the substrate by substituting a small fraction, y, of the potassium with sodium, thereby yielding a good substrate-film interface and a film surface that does not need polishing, resulting in high quality films with low optical losses. Additionally, for electro-optic applications the ratio x between niobium and tantalum allows the phase transition between the cubic paraelectric and tetragonal ferroelectric phases to be shifted close to the temperature of operation following an almost linear dependence (see Fig. 1.7), thereby exploiting large EO coefficients of several hundred pm/V.

### 3.2.2 Bulk and thin film growth and waveguide preparation

The cubic KNTN bulk and thin film material described in this work was grown with a material composition of $x = 0.34 \pm 0.01$, resulting in an expected Curie point T_c around -80 °C according to Gutmann [72]. The Na content $y = 0.02 \pm 0.01$ was then chosen to achieve the best possible lattice-matching between the KT substrate and the thin film. Bulk KNTN crystals were grown in high temperature solution using the Czochralski pulling method. The growth procedure is similar to that reported for KT in a recent publication [73].

The KNTN thin films of a few microns thickness were grown by liquid phase epitaxy (LPE) onto polished (< 5 nm RMS roughness) KT substrates with a typical size of $1 \times 1 \times 0.2$ cm^3. By performing the growth at a low level of supersaturation, resulting in a slower growth rate, and utilizing a technique that allows for very precise temperature control (± 0.1 °C) in the growth furnace, optically flat film surfaces have been achieved for the first time to our knowledge without the need for surface polishing. The remaining relative lattice mismatch was measured to be smaller than 1×10^{-4} as confirmed by XRD. Details of the growth procedure will be reported elsewhere. The surface quality was determined by AFM measurements on areas of 100 x 100 μm^2 and was found to exhibit no height variations exceeding 90 nm over the scan range with an RMS roughness of 21 nm. Three surface profile plots and the
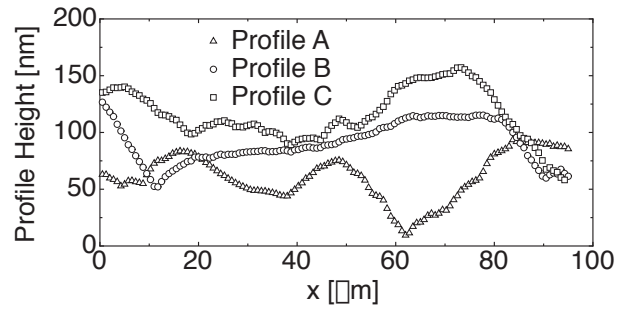
(a)
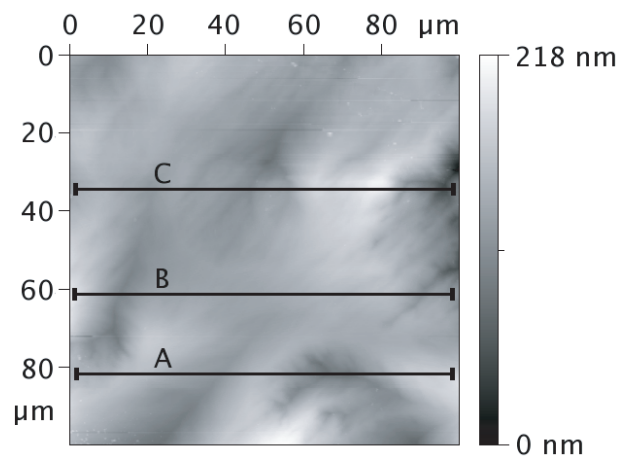
(b)

Figure 3.1: (a): AFM surface profiles of an as-grown potassium sodium tantalate niobate thin film of thickness $d = 1.4$ μm epitaxially grown on a potassium tantalate substrate. Scans over 100 μm show an RMS roughness of 21 nm with maximum height variations of 90 nm. (b): AFM surface scan of the thin film surface. The horizontal lines indicate the positions of the profiles in Fig. 3.1(a).

AFM image that they were derived from are shown in Fig. 3.1(a) and Fig. 3.1(b), respectively. After end face polishing, laser light was coupled with a 20 x microscope objective into the slab waveguide, whose core consisted of the KNTN film having a higher refractive index than the KT substrate. Waveguiding was tested by using lasers with the following wavelengths: $\lambda = 532, 633, 860, 980, 1330$ and 1550 nm. The output facet was imaged with a 100 x objective onto an Allied Dolphin F-145B 12 bit b/w CCD camera. Fig. 3.2 shows the intensity distribution of a guided TM mode at $\lambda = 532$ nm.
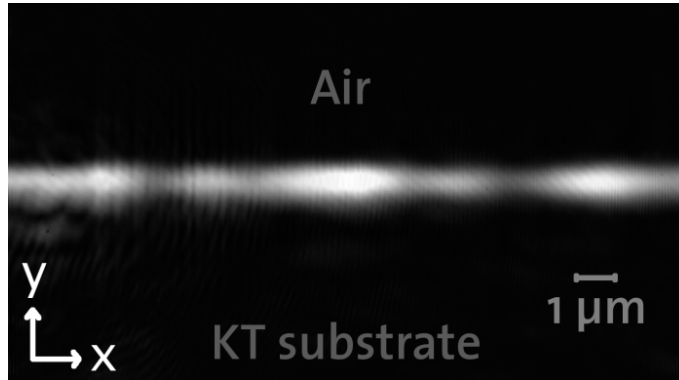

Figure 3.2: Image of the TM light transmitted by the slab waveguide consisting of a potassium sodium tantalate niobate film on a potassium tantalate substrate at $\lambda = 532$ nm. The film thickness and refractive index contrast are $d = 1.4$ μm and $\Delta n = 8 \times 10^{-3}$, respectively.

As a result of the designed, and subsequently confirmed, monomodality of the waveguide, the increased complexity of prism coupling did not promise to provide any beneficial information on the guided wave propagation and thus was not performed.

3.2.3 Material characterization

The thickness d of the film and the refractive index contrast Δn between KNTN film and KT substrate were obtained by comparing the measured light intensity along a vertical cross section of the waveguide output with the solution of the optical TM mode of a slab waveguide. The latter can be derived by solving the Helmholtz equation:

$$\frac{d^2 H_x(y)}{dy^2} + k_0^2(n^2(y) - N^2)H_x(y) = 0 \tag{3.1}$$

$$n(y) = \begin{cases} 1 & y > 0 \\ n_{KT} + \Delta n & -d < y \leq 0 \\ n_{KT} & y \leq -d \end{cases} \tag{3.2}$$

where $H_x(y)$ is the component of the magnetic field along the x axis, $n(y)$ is the refractive index, $n_{KT} = 2.233$ is the refractive index of the bulk KT material at $\lambda = 0.633$ μm, N is the mode effective index, $k_0 = 2\pi/\lambda$, and d is the film thickness.

For every set of the free parameters d, N and Δn the equation is solved (with the proper TM boundary conditions at $y = 0$ and $y = -d$, i.e. the continuity of H_x and $1/n_x^2 dH_x/dy$) and the resulting theoretical intensity $I(y) \propto |H_x(y)|^2$ is compared to the measured light intensity. Using a least-square error algorithm, the parameters were determined to be $d = 1.4 \pm 0.2$ μm and $\Delta n = (8 \pm 3) \times 10^{-3}$ at $\lambda = 633$ nm. The comparison between the theoretical and experimental profiles for these values is depicted in Fig. 3.3, showing good agreement.
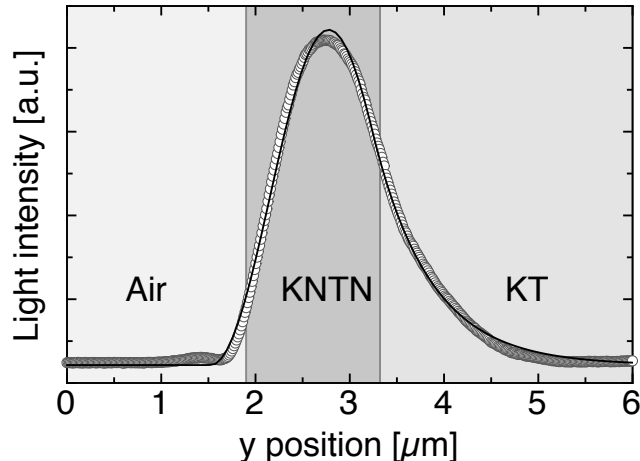

Figure 3.3: Measured light intensity (open circles) along a vertical (y) cross section of the planar waveguide in a potassium sodium tantalate niobate thin film on a potassium tantalate substrate. The solid line represents the best-fitting theoretical solution of the Helmholtz equation with waveguide thickness $d = 1.4 \pm 0.2$ μm and refractive index contrast $\Delta n = (8 \pm 3) \times 10^{-3}$ at $\lambda = 633$ nm.

Mode propagation calculations performed with the OlympIOs software package from C2V, Netherlands, showed that waveguides with this thickness and index contrast should support guided modes up to the cut-off wavelength $\lambda_{co} = 1.05$ μm. This was confirmed experimentally as waveguiding could be observed for $\lambda = 532, 633, 860$ and 980 nm, but not for 1330 and 1550 nm. Thicker films will therefore be needed in order to support waveguiding at telecom wavelengths.

The optical losses of the slab waveguide were estimated by taking the ratio between the optical power before the first and after the second microscope objective. The upper limit of the waveguide losses is 18 dB/cm at $\lambda = 633$ nm. However, great uncertainty exists with respect to the coupling efficiency and losses stemming from imperfect facet preparation, and therefore, we expect the real propagation loss in a properly polished sample to be well below 10 dB/cm.

Refractive index values were compared to those of bulk KT and KNTN by utilizing cut and polished crystals of pure KT and KNTN that were analyzed with a femtosecond time delay refractive index setup [74]. The refractive index dispersion of both materials is displayed in Fig. 3.4 and a contrast of $\Delta n \approx (2.6 \pm 0.3) \times 10^{-2}$ for $\lambda = 633$ nm was deduced, resulting in a three-fold increase compared to the observed Δn of the thin film. The reason for this discrepancy is discussed in the next section.
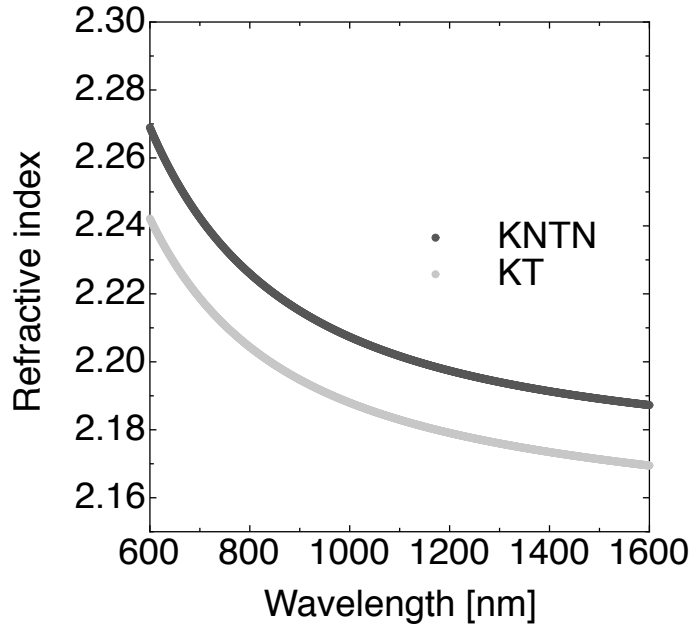
Figure 3.4: Dispersion curves of bulk cubic potassium tantalate and potassium sodium tantalate niobate measured at room temperature with the femtosecond pulse time delay method. The contrast Δn between the indices of bulk potassium tantalate and potassium sodium tantalate niobate at $\lambda = 633$ nm is about $(2.6 \pm 0.3) \times 10^{-2}$.

In order to measure the permittivity of bulk and thin film KNTN, interdigital electrodes of 40 nm gold on top of 10 nm chromium (acting as adhesion promoter) were deposited on the bulk or thin film crystal surface by standard photolithography processing, electron beam metal deposition and a standard lift-off process [75]. The layout of the electrodes is shown in Fig. 3.5, and consists of ten 5 μm-wide fingers overlapping over a length of $L = 2$ mm, spaced 5 μm apart. These finger electrodes allow the dielectric properties of thin films to be measured locally and with a well defined contribution of the substrate. A simulation model of the system was created in Comsol Multiphysics that calculates the capacitance of the electrode system as a function of thickness and permittivity of the film as well as the permittivity of the substrate. Using this model, the relative permittivity of the thin film was then deduced from the measured capacity. All dielectric measurements were taken with an HP 4192 impedance analyzer connected to the interdigital electrodes at $f = 10$ MHz. The crystals were placed in an evacuated helium cryostat, controlled by a Lakeshore 330 auto-tuning temperature controller.

The relative dielectric permittivity of both bulk and thin film KNTN as a function of temperature is shown in Fig. 3.6. As substantiated by the graph, the bulk material has a phase transition between the cubic paraelectric and tetragonal ferroelectric phase, occurring at $T_c = -79 \pm 0.5\,°C$. The permittivity reaches a maximum value of $\varepsilon \approx 13'000$ at this point. The permittivity at room temperature is about $\varepsilon \approx 750$.

By contrast, the thin film KNTN shows a much wider and shallower peak displayed in Fig. 3.6. The maximum lies around -80 °C and the permittivity reaches
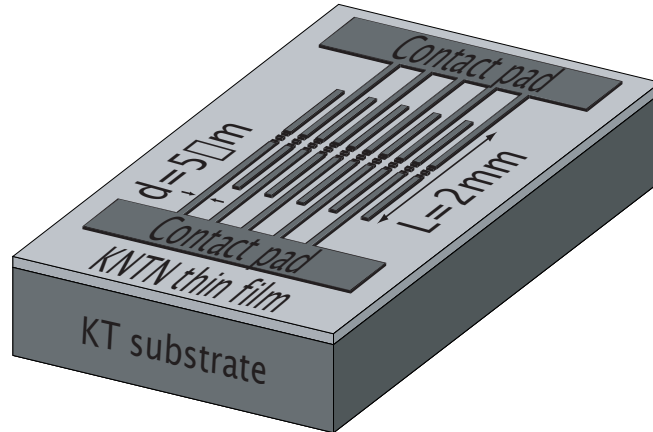
Figure 3.5: Layout of the interdigital electrodes used for the permittivity measurements on potassium sodium tantalate niobate thin films (shown here), bulk potassium tantalate, and bulk potassium sodium tantalate niobate.
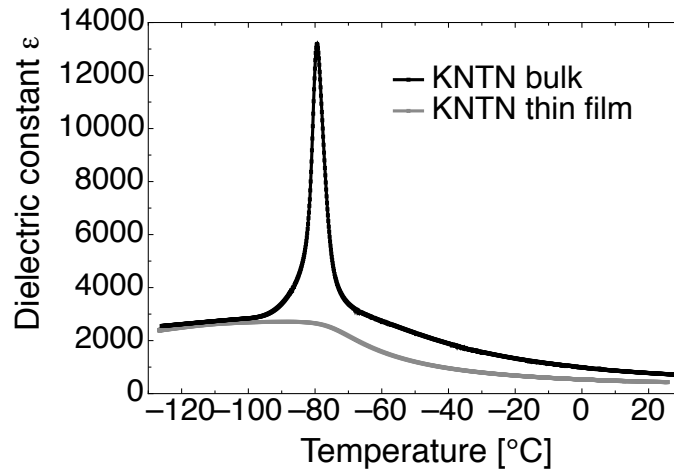
Figure 3.6: Relative dielectric permittivity of a $K_{1-y}Na_yTa_{0.66}Nb_{0.34}O_3, y \approx 0.02$ bulk (dark line) and epitaxial 1.4 μm thin film (light line) sample as a function of temperature, measured at $f = 10$ MHz using interdigital electrodes connected to an HP4192 impedance analyzer. The permittivity exhibits a maximum at $T_c \approx -79 \pm 1$ °C.

$\varepsilon \approx 2700$, with a room temperature value of $\varepsilon \approx 440$. Additionally, the Curie temperature T_0 can be extracted from the well-known Curie-Weiss law

$$\varepsilon = \frac{C}{T - T_0}$$

where C is the Curie constant and $T > T_c$. The linear extrapolation of $1/\varepsilon$ yields a $T_0 \approx -91 \pm 0.5$ °C, which is lower than T_c as could be expected for a first-order phase transition.

As in the case of the refractive indices, the thin film values are considerably lower than those of the bulk. This difference is further confirmed by the resistivity at the phase transition temperature: while the resistivity between the electrode fingers decreases to 0.04 Ωm in the bulk, it is always larger than 25 Ωm in thin films.

3.3   Discussion

The fundamental suitability of the system for optical waveguiding applications has been proven, and from the dielectric measurements the quadratic electro-optic coefficient R of the KNTN thin film can be estimated as follows:

$$R = \varepsilon_0^2 (\varepsilon - 1)^2 g$$

where $\varepsilon_0 \approx 8.854 \times 10^{-12}\,\mathrm{Fm^{-1}}$, ε is the permittivity of the material and g is a material parameter that is quite constant over temperature and a wide range of perovskite materials [76]. For the KT material family $g \approx 0.14\,\mathrm{m^4 C^{-2}}$ which results in $R \approx 2.1 \times 10^{-18}\,\mathrm{m^2 V^{-2}}$ at 20 °C and $R \approx 8 \times 10^{-17}\,\mathrm{m^2 V^{-2}}$ at -79 °C.

While the prospects towards electro-optic applications are promising, there are some remaining issues that have to be addressed in order to be able to fully exploit all of the system's advantages: namely the reduction in refractive index and permittivity of the KNTN film as compared to the bulk. Resistivity measurements and previous studies [72] suggest that this could be due to oxygen deficiencies in the film as they generate Schottky defects, resulting in a reduced density of the material and n-type hopping semiconductivity. In fact a diode-like behavior of the IV characteristic of some films coated with painted silver electrodes could be observed.

The broadening of the permittivity peak at T_c is believed to originate from regions with slightly different Ta-Nb ratios, giving rise to a diffuse phase transition.

3.4   Conclusion

Monomodal slab waveguiding in epitaxial as-grown flat cubic KNTN thin films on KT substrates at wavelengths between 532 and 980 nm has been demonstrated for the first time. The film thickness $d = 1.4 \pm 0.2$ μm and refractive index contrast $\Delta n = (8 \pm 3) \times 10^{-3}$ at $\lambda = 633$ nm have been determined. Even with refractive index and permittivity values not fully on par with those of the bulk material, the successful demonstration of waveguiding in these films represents a very important step towards the use of lattice-matched epitaxially grown KNTN thin films on KT

substrates in electro-optical applications without the need for surface polishing. Experiments are currently under way to try to either post-oxidize the films after growth or to directly incorporate more oxygen during epitaxy.

Chapter 4

Electro-optic phase modulation in ridge waveguides of epitaxial $\mathbf{K}_{0.95}\mathbf{Na}_{0.05}\mathbf{Ta}_{0.71}\mathbf{Nb}_{0.29}\mathbf{O}_3$ thin films[†]

Electro-optic modulation at $\lambda = 1.5$ μm has been demonstrated for the first time to the best of our knowledge in a ridge waveguide phase modulator produced in cubic potassium sodium tantalate niobate thin films epitaxially grown on potassium tantalate substrates exploiting the large quadratic electro-optic Kerr coefficient of $R_{11} = 8.2 \times 10^{-17}$ m^2/V^2. The relative permittivity, Kerr coefficient, and refractive index have been evaluated for the thin film crystal and are compared to the values measured in bulk crystals. The half-wave voltage times length figure of merit of the modulator has been measured to be $V_\pi\,l = 38$ Vcm at room temperature.

4.1   Introduction

In recent years, electro-optic crystals of the potassium tantalate niobate (KTN) family have attracted increased attention for integrated optics due to its large linear and quadratic electro-optic coefficients [31] and the possibility of tuning the phase transition temperature by varying the Ta:Nb ratio [78, 72, 79, 80]. The latest achievements in this field include the growth of nonlinear optical thin films of KTN on GaAs by pulsed laser deposition [81], electro-optic devices in buried KTN waveguides [69], and a wide-angle KTN beam deflector [82]. For guided optics applications, epitaxially grown thin films promise to combine low optical losses with bulk-like dielectric and electro-optic properties as long as two requirements are met: good lattice matching at the substrate-film interface and an optically flat thin film surface. While other groups have reported KTN thin films on GaAs [81] or MgO [83] substrates, as well as KTN waveguides embedded in KTN of different composition [69], we have recently demonstrated a technique that we think combines the advantages of a good substrate-film interface and an optically flat thin film surface [29]. The liquid-phase

---

[†]An abbreviated version of this chapter has been published in Optics Express [77].

epitaxial growth of thin films of potassium sodium niobate tantalate (KNTN) on KT substrates with an as-grown optically flat surface, slab waveguiding therein and the measurement of the optical and dielectric properties of these films have been described in this publication. By substituting a small percentage of the potassium with sodium and performing the growth at a slow growth rate, a very small relative lattice mismatch of less than 1×10^{-4} and an RMS surface roughness of approximately 20 nm were achieved.

To the best of our knowledge, we present for the first time ridge waveguiding and electro-optic modulation in KNTN thin films on KT substrates at infrared wavelengths in this paper, exploiting the huge quadratic electro-optic coefficient in this material. In the first part of this work, the material composition and dielectric behavior around the phase transistion temperature are assured by Rutherford back scattering (RBS) and interdigital electrode impedance measurements, respectively. In a bulk KNTN crystal, the quadratic electro-optic coefficient was measured in a cryostat interferometer setup and related to the dielectric behavior of the specimen. In μm-thick epitaxial films of KNTN grown on KT, ridge waveguides were produced by photolithography and argon-ion etching. The waveguides were characterized in terms of refractive indices and propagation losses, using a mode profile reconstruction method and a Fabry-Perot loss measurement technique, respectively. The loss values obtained at $\lambda = 1.55$ nm are put into perspective by the exponential decay of the scattered light intensity at HeNe wavelength. Using photolithography, electron-beam metal deposition and lift-off techniques, side electrodes were deposited parallel to the waveguides in order to create an integrated electro-optic phase modulator. The performance of this modulator was tested in terms of half-wave voltage V_π and modulation frequency.

4.2 Materials, growth and electrical properties

Potassium tantalate niobate ($KTa_{1-x}Nb_xO_3$, abbreviated KTN) is a solid solution of the two materials potassium tantalate (KT) and potassium niobate (KN). Depending on the ratio x between tantalum and niobium, the Curie temperature T_0 of the phase transition between the paraelectric cubic phase and the ferroelectric tetragonal phase can be gradually shifted from 0 K for pure KT ($x = 0.0$) to 710 K for pure KN ($x = 1.0$) [1]. KTN was studied extensively and has been epitaxially grown on a variety of substrates [83, 81, 69], but the quality of the substrate-film interface is largely determined by the lattice mismatch between the substrate and thin film materials and even the use of several buffer layers produced relative mismatch values in the low percent range [81]. In Section 3.2.2 we haven shown that by substituting a small percentage y of the potassium with sodium, an excellent lattice matching (relative mismatch $< 1 \times 10^{-4}$) between the KT substrate and the $K_{1-y}Na_yTa_{1-x}Nb_xO_3$ thin film can be achieved that results in a good interface and a thin film surface that does not require polishing to be suitable for integrated optical applications.

Since our first waveguiding KNTN thin films (see Chapter 3), the KNTN material composition has been modified from $K_{0.98}Na_{0.02}Ta_{0.66}Nb_{0.34}O_3$ (called KNTN1) to $K_{0.95}Na_{0.05}Ta_{0.71}Nb_{0.29}O_3$ (KNTN2, see Fig. 4.1) to shift the phase transition
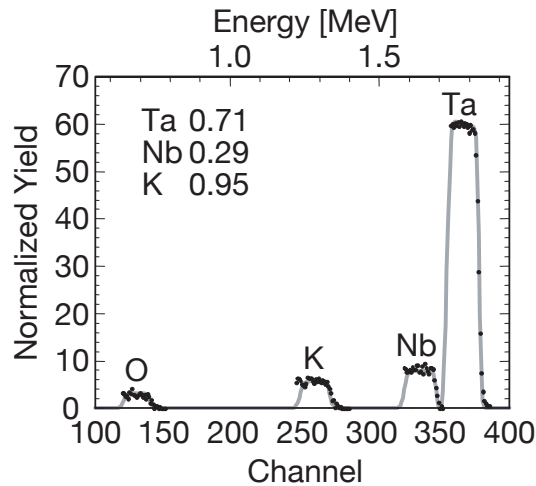
Figure 4.1: Rutherford back scattering measurement on epitaxial thin film of potassium sodium niobate tantalate grown on potassium tantalate substrate. The analysis yields a material composition $K_{0.95}Na_{0.05}Ta_{0.71}Nb_{0.29}O_3$.

closer to room temperature which significantly increases the relative dielectric permittivity ε and the quadratic electro-optic coefficient R, since the relative dielectric permittivity theoretically diverges at T_0 according to the Curie-Weiss law

$$\varepsilon = \frac{C}{T - T_0},$$

$$(4.1)$$

where C is the Curie constant and $T > T_0$, and the quadratic electro-optic Kerr coefficient R is related to ε according to

$$R = \varepsilon_0^2(\varepsilon - 1)^2 g,$$

$$(4.2)$$

where $\varepsilon_0 \approx 8.854 \times 10^{-12}\,\mathrm{F\,m^{-1}}$, ε is the relative permittivity of the material and the quadratic polarization-optic coefficient g is a material parameter that is mainly determined by the oxygen octahedron in perovskites and therefore is almost constant as a function of temperature and varies only by a factor of 2-3 in different perovskites.

There are two main reasons why we didn't use KNTN with a Curie temperature above room temperature which would allow us to exploit the larger linear electro-optic Pockels coefficient r: first of all, perovskites exhibit domains in the ferroelectric phase which require poling and might give rise to scattering losses. Secondly, the waveguide phase modulator presented in this paper relies on the simultaneous propagation of both TE and TM modes in the waveguide with similar properties, which is only possible in an optically isotropic material like cubic KNTN. For future applications, work has however been started to grow ferroelectric KNTN thin films on KT substrates doped with barium, which significantly increases the electric conductivity of the KT and allows it to be used as a bottom electrode for poling and to apply the electric field to induce the electro-optic effect.

Using the growth process already described in Chapter 3, paraelectric thin films of

KNTN of a few micrometers were grown in liquid-phase epitaxy (LPE) on cubic KT substrates of typically 1 cm × 1 cm × 0.2 cm dimensions. The material quality of the thin film could be significantly enhanced through optimization of the growth parameters, as substantiated in Fig. 4.2. The graph shows the relative dielectric permittivity of the thin films, measured with an HP 4192 impedance analyzer connected to interdigital electrodes deposited on the thin film surface. It can be seen that the present films (in black) show a phase transition temperature of $T_c \approx -10\,°C$ and exhibit a much higher dielectric permittivity than the previous samples (in gray). The relative dielectric permittivity reaches $\varepsilon = 4000$ at the phase transition temperature and $\varepsilon = 2100$ at room temperature. As described later in this paper, the refractive index of the thin film material could also be noticeably increased. These improvements resolve the major limitation we addressed in Chapter 3: the distinct difference in material properties between bulk and thin film KNTN.
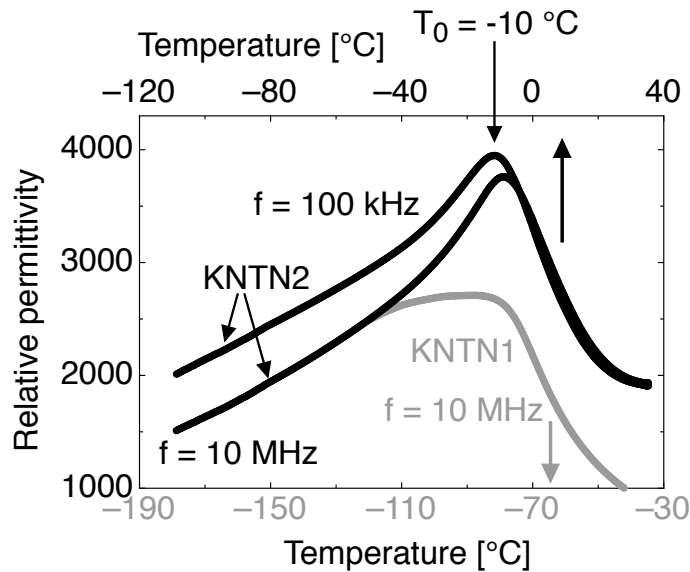
Figure 4.2: Relative permittivity of potassium sodium niobate tantalate thin film epitaxially grown on potassium tantalate substrate as a function of temperature and frequency. Black curve shows improved material quality of present film compared to the one from our previous study (Chapter 3, gray curve).

The quadratic electro-optic coefficient R_{11} was measured in a bulk crystal of composition KNTN1 in a cryostatic interferometer setup (depicted in Fig. 4.3 and described in detail in Appendix A) in order to relate it to the values deduced from the modulator performance. Problems were encountered from low-frequency phase variations (probably emanating from local structural changes in the material) at cryogenic temperatures that impeded a stable fixation of the working point, but this could be compensated by an active phase control (APC).

The temperature dependence of R_{11} measured in the interferometer setup can be used to deduce the quadratic polarization-optic coefficient g_{11} and the Curie

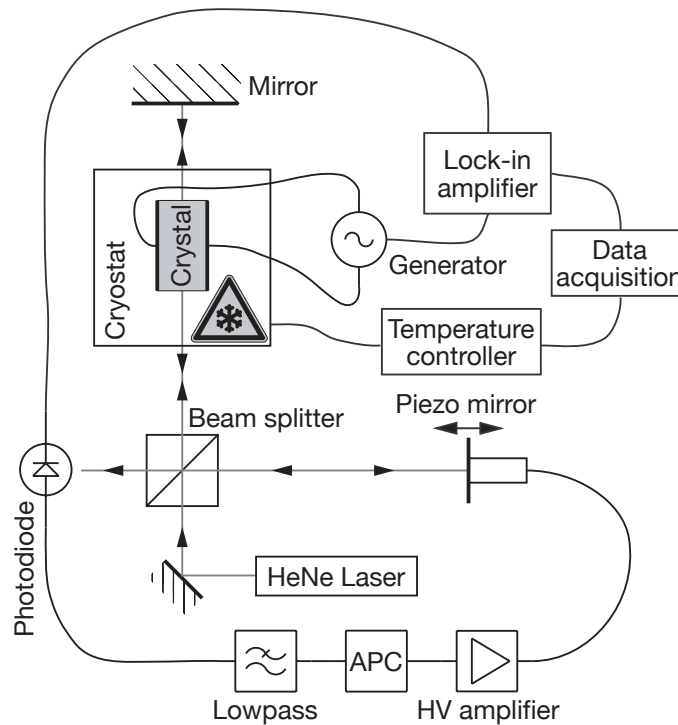Figure 4.3: Cryostatic interferometer setup to measure the quadratic electro-optic coefficient R_{11} of potassium sodium niobate tantalate bulk crystals. Low-frequency phase oscillations are compensated by an active phase control.

temperature T_0 according to

$$R_{11} = \varepsilon_0^2 \frac{C^2}{(T-T_0)^2} g_{11}. \qquad (4.3)$$

Fig. 4.4 displays the measured R_{11} values, the least-squares error approximation of equation (4.3) with the fit values $T_0 = -81.1$ °C and $g_{11} = 0.17$ m^4 C^{-2} and the R_{11} values calculated from dielectric permittivity measurements of our last publication, showing good agreement. The Curie constant of $C = 5.8 \times 10^4$ K was also taken from the permittivity data of KNTN1. The wider divergence of the curve derived from the dielectric measurements can probably be explained by the following: a bigger part of the volume of the crystal contributes to the coefficient deduced from the dielectric permittivity when compared to the more local probing of the laser beam in the interferometer, leading to a somewhat diffused phase transition. A similar effect has been observed in the past when comparing phase transition curves measured with plate versus interdigital electrodes [29]. The value of $g_{11} = 0.17$ m^4 C^{-2} lies between the values reported by Geusic [76] ($g_{11} = 0.136$ m^4 C^{-2}) and Buse [84] ($g_{11} = 0.211$ m^4 C^{-2}). Note that the bulk crystal was grown with the older composition and a lower phase transition temperature, but the composition dependence of g_{11} given by Buse [84] allows us to adapt the results to the new composition and therefore the lengthy process of growing good quality bulk crystals of KNTN2 composition was not performed.

To summarize, we can say that quadratic electro-optic coefficients of $R_{11} \approx 2.5 \times$
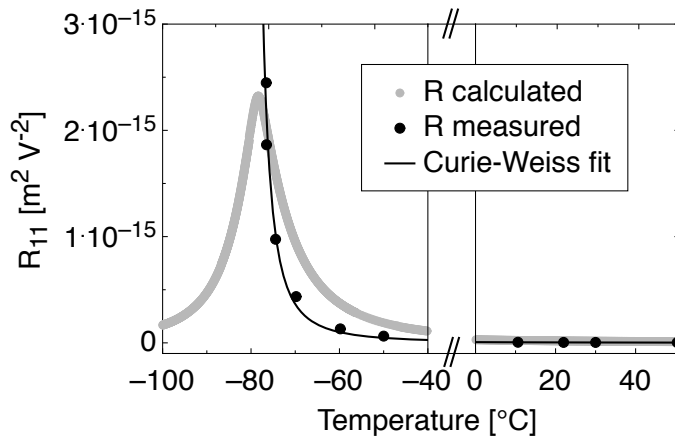
Figure 4.4: Quadratic electro-optic Kerr coefficient R_{11} of potassium sodium niobate tantalate bulk crystal as a function of temperature. Black points represent values measured by the interferometer setup, solid black curve indicates Curie-Weiss law and solid gray curve represents R_{11} calculated from dielectric permittivity data.

$10^{-15}\,\mathrm{m^2\ V^{-2}}$ at the phase transition temperature and up to $R_{11} \approx 2 \times 10^{-16}\,\mathrm{m^2\ V^{-2}}$ at $T = T_0 + 30$ °C, which corresponds to room temperature for our present films, are the upper limit set by the bulk values and are by any means high enough to justify the production of an electro-optic device.

4.3 Waveguide production and characterization

With KNTN thin films of good optical quality and high Kerr coefficients at hand, the next step was the production of ridge waveguides and their characterization. To this end, waveguides of nominal widths of $3, 5, 7, 9$ and 11 μm were structured into the commercial photoresist AZ6632 and then transferred to the KNTN thin film by argon ion etching. Scanning electron microscopy (SEM), atomic force microscopy (AFM) and optical microscopy pictures confirmed an etch depth of $h = 3.4\pm0.1$ μm. After polishing of the crystal facets, infrared light from a Santec TSL-210 laser at $\lambda = 1579$ nm was coupled into the waveguides using a microscope objective. The output of the waveguide was imaged with a 100 x objective onto a Sensors Unlimited SU320MX-1.7RT infrared InGaAs CCD camera. Fig. 4.5 shows an overlay of the waveguide cross section of a 7 μm wide ridge, uniformly illuminated from the back, and the TE mode guided in the waveguide. The inset on the left depicts the simulation of the propagating mode and will be discussed later.

Starting from a vertical cut through the intensity distributions of the guided TE and TM modes, we employed the profile reconstruction method described in Chapter 3 to derive the thickness d of the film and the refractive index contrast Δn between KNTN film and KT substrate. The method works by solving the Helmholtz equation for guided modes as a function of the film thickness d and the refractive index distribution $n(y)$, and minimizing error between the measured intensity distribution and the theoretical function using a least-square error algorithm. Since the width

Figure 4.5: Waveguide profile and TE mode intensity distribution of $\lambda = 1579$ nm laser light propagating in a potassium sodium niobate tantalate thin film ridge waveguide. Left inset shows simulated mode profile with excellent agreement to measurement.

$w = 7$ μm of the waveguide is much larger than the wavelength $\lambda = 1579$ nm, the intensity distribution in y direction can be approximated by a guided slab mode. The result for a TE mode is shown in Fig. 4.6 and shows an excellent agreement. The parameters were determined to be $d = 3.4 \pm 0.1$ μm and $\Delta n = (11.0 \pm 1.5) \times 10^{-3}$.
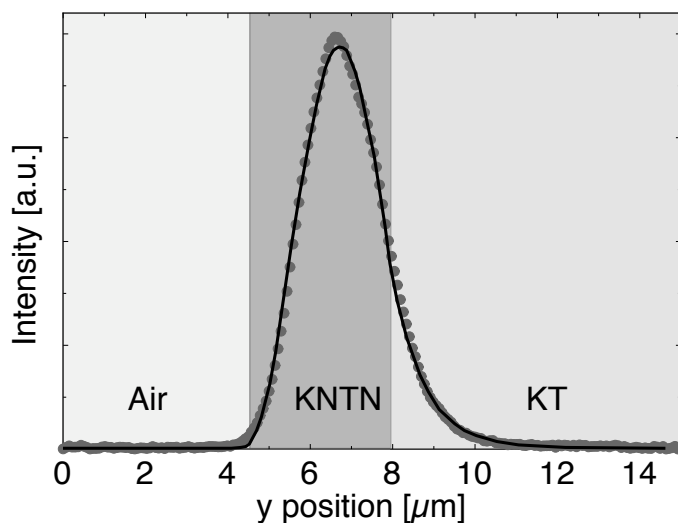
Figure 4.6: Measured light intensity (gray circles) along a vertical (y) cross section of potassium sodium niobate tantalate thin film ridge waveguide on potassium tantalate substrate. Solid curve represents the best-fitting theoretical solution of the Helmholtz equation with thin film thickness $d = 3.4 \pm 0.1$ μm and refractive index contrast $\Delta n = (11.0 \pm 1.5) \times 10^{-3}$.

Both this refractive index contrast of $\Delta n = (11.0 \pm 1.5) \times 10^{-3}$ and the result of the dielectric permittivity measurement confirm that the present thin film has dielectric and optical properties almost on par with the bulk material. Fig. 4.7 shows the dispersion curves of bulk KT and KNTN, and the thin film values of the last (at 633 nm) and the present (at 1579 nm) thin films, indicating that bulk values

could almost be reached in present films.

Using the geometry and refractive index values as reported here, we performed a simulation of the propagating TE waveguide mode with the commercial OlympIOs software package [52]. The resulting mode intensity distribution is shown on the left side of Fig. 4.5, demonstrating excellent consistence between measurement and simulation.
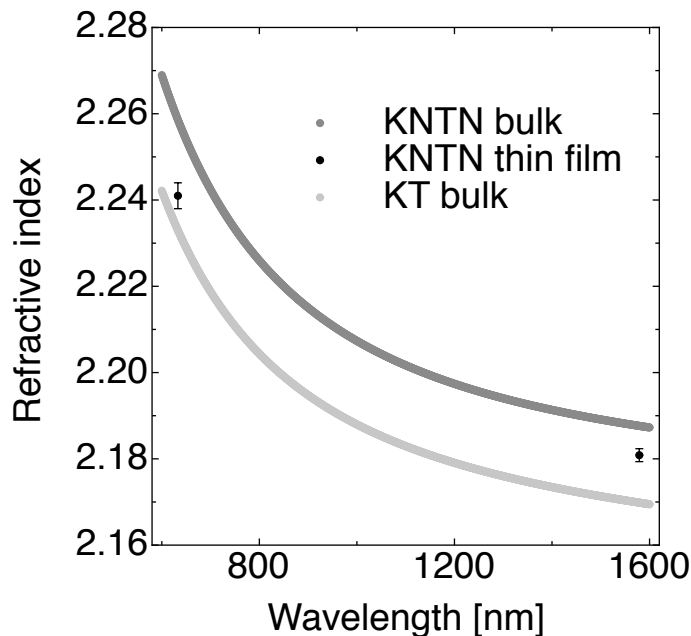

Figure 4.7: Refractive index dispersion of bulk potassium tantalate (light gray solid curve), bulk potassium sodium niobate tantalate (dark gray solid curve), and epitaxial potassium sodium niobate tantalate thin film (solitary points). The thin film refractive index at $\lambda = 1579$ nm is almost equal to the bulk value.

Two methods were used to determine the losses of the waveguides: the Fabry-Perot resonator and the scattered light technique. For the resonator method, we exploit the fact that the wavelength-dependent transmission of the waveguide with its end facets acting as a Fabry-Perot resonator shows resonances whose finesse is directly related to the losses in the resonator. The measured transmitted intensity versus wavelength around $\lambda = 1561$ nm is depicted in Fig. 4.8 and can be described by

$$T(\lambda) = \frac{T_{max}}{1 + (\frac{2\mathcal{F}}{\pi})^2 \sin^2(\frac{2\pi L n}{\lambda} + \phi)}, \tag{4.4}$$

where T_{max} is the maximum output intensity, $\mathcal{F}$ is the finesse of the resonator, $L = 4.68$ mm is the resonator length, n is the effective index of the propagating mode and ϕ is a random phase. This analytical function can be fitted to the measured transmission with $\mathcal{F}$, T_{max}, n, and ϕ as parameters. The result of the fitting process is also shown in Fig. 4.8 and yields a finesse of $\mathcal{F} \approx 0.55$.
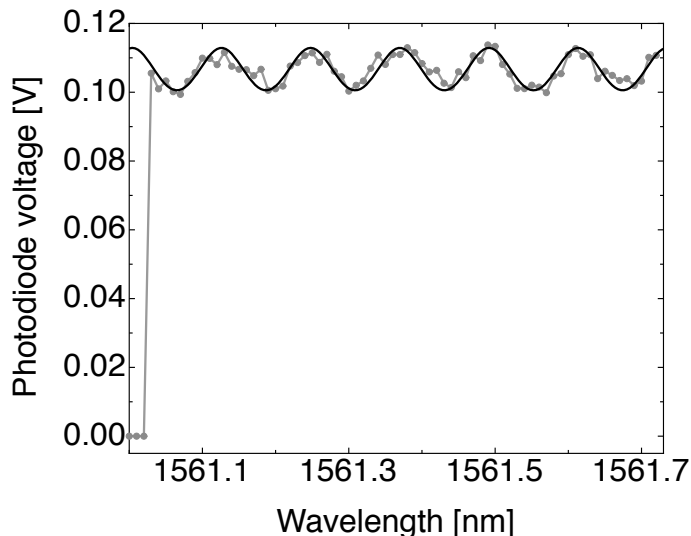
Figure 4.8: Fabry-Perot resonances at $\lambda = 1561$ nm in potassium sodium niobate tantalate thin film ridge waveguide on potassium tantalate substrate with the facets acting as mirrors. A finesse $\mathcal{F} \approx 0.55$ yields an upper limit for TE propagation losses of 14 dB/cm assuming perfect facets.

The resonator finesse $\mathcal{F}$ can be related to the propagation loss factor α in the waveguide and the mirror losses R via

$$\mathcal{F} = \frac{\pi \sqrt{R} \cdot e^{-\alpha L/2}}{1 - R \cdot e^{-\alpha L}} \tag{4.5}$$

Assuming perfect facets with Fresnel reflection losses as the only loss mechanism, we obtain a loss factor of $\alpha \approx 3.3$ cm^{-1}, which corresponds to 14 dB/cm. While this value marks the upper limit of the propagation losses, the assumption of perfect facets is obviously not true and the actual propagation losses are much lower. This is demonstrated by imaging the scattered light along propagation of a guided TE mode at $\lambda = 633$ nm onto an Allied Dolphin F-145B 12 bit b/w CCD camera. Since the scattered intensity is proportional to the local power in the waveguide and the linearity of the optical system including the software was assured, the measured intensity as a function of propagation distance follows an exponential decay law with the loss coefficient α in the exponent. The result of this measurement is shown in Fig. 4.9 and yields propagation losses of 7.8 ± 0.5 dB/cm for $\lambda = 633$ nm. Since scattering losses decrease with increasing wavelength, the propagation loss value for infrared wavelengths is believed to be smaller. The measurement was performed at HeNe wavelength since no high-resolution camera was available for $\lambda = 1.5$ μm. The relatively high propagation losses can be attributed to the roughness of the etched sidewalls (RMS roughness approximately 55 nm) and the high refractive index contrast at these interfaces. Possible measures to reduce the losses will be discussed in Section 4.5. In terms of both propagation constants and losses, TE and TM modes are equal within the experimental error and no mode mixing was observed, which allows for the fabrication of a waveguide phase modulator.
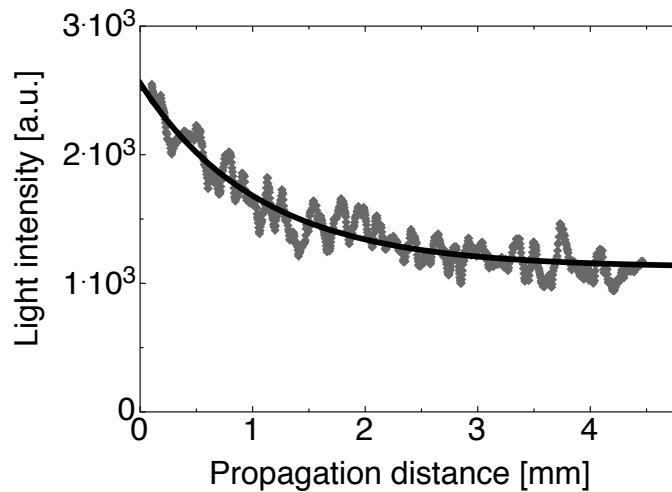
Figure 4.9: Measured scattered light intensity at $\lambda = 633$ nm (gray curve) along propagation in potassium sodium niobate tantalate thin film ridge waveguide on potassium tantalate substrate. Exponential decay fit yields propagation losses of 7.8 ± 0.5 dB/cm (black curve).

4.4   Electro-optic phase modulator

Using the polarization-maintaining ridge waveguides described above, an integrated electro-optical phase modulator was created by depositing parallel electrodes on either side of a 7 μm wide waveguide. If light is coupled at an angle of $45\,^{\circ}$ to the horizontal into the waveguide, both the TE and TM modes are excited inside the waveguide and propagate independently. By applying a voltage to the electrodes, the resulting electric field in the waveguide core shifts the phase of one polarization with respect to the other due to the electro-optic effect. This phase difference is converted into an amplitude change by an analyzer at the output. An additional compensator allows to set the working point of the modulator. A schematic of the setup is shown in Fig. 4.10. Microscope objectives were used to couple the light into and out of the waveguide. Electrodes consisting of 50 nm gold on top of 10 nm chromium (acting as adhesion promoter) were deposited on the thin film surface by standard photolithography processing, electron beam metal deposition, and a standard lift-off process. The distance between the electrodes is $s = 16$ μm, with the waveguide in the middle.

The half-wave voltage V_π, defined as the voltage needed to switch the modulator from minimum to full intensity or vice versa, is the key figure of merit for a modulator and allows us to assert the electro-optic coefficient R values discussed earlier. V_π was measured by adjusting the compensator to full darkness at the modulator output and then recording the transmitted light intensity as a function of the DC voltage applied to the electrodes. The resulting graph is shown in Fig. 4.11 and yields $V_\pi = 99 \pm 2$ V for an electrode length of $l = 3.8$ mm. Possible methods for reducing this value are discussed in Section 4.5.

To calculate the electro-optic coefficient R, the strength of the electric field at $V_\pi = 100$ V inside the waveguide core is needed. A Comsol Multiphysics model of the
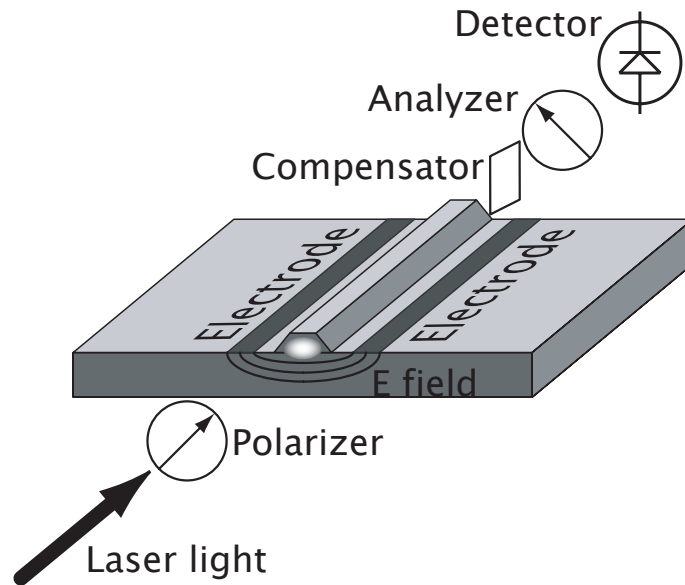
Figure 4.10: Schematic of the setup used to characterize the potassium sodium niobate tantalate thin film ridge waveguide phase modulator working at $\lambda = 1550$ nm.
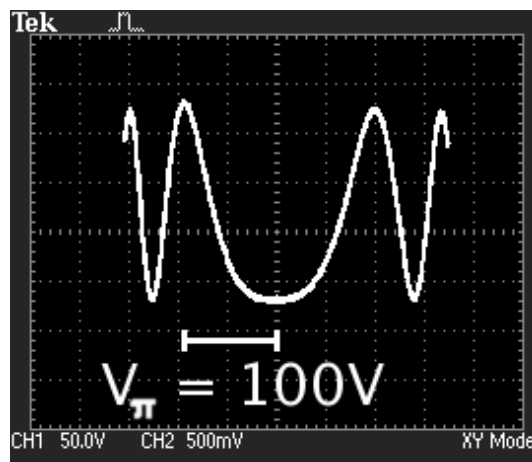

Figure 4.11: Transmitted light intensity (y-axis) at $\lambda = 1550$ nm in potassium sodium niobate tantalate thin film ridge waveguide phase modulator as a function of DC voltage applied to parallel side electrodes (x-axis). Graph shows a half wave voltage of $V_\pi \approx 100$ V.

modulator cross-section was created (see Fig. 4.13) with the geometry and dielectric permittivity values obtained previously. The simulation shows that (1) the electric field is rather uniform in the waveguide core area with a value of $E_x \approx 0.7 \times 10^6$ V/m and (2) the horizontal component E_x of the electric field is about 40 times stronger than the vertical E_y. At V_π, electric field strength and Kerr coefficients are related by

$$R_{11} E_x^2 - R_{12} E_y^2 = \frac{\lambda}{n^3 \, l},$$ (4.6)

where $\lambda = 1550$ nm is the wavelength, $l = 3.8$ mm is the length of the electrodes and $n = 2.18$ is the effective mode index. In our case $E_y \ll E_x$ and thus, equation (4.6) is reduced to

$$R_{11} = \frac{\lambda}{n^3 \, E_x^2 \, l}.$$ (4.7)

Using $E_x \approx 0.7 \times 10^6$ V/m in the equation above yields $R_{11} \approx 8.2 \times 10^{-17}$ m^2/V^2. This is about 40% of the expected bulk value and very high compared to other materials. Utilizing the following expression,

$$\varepsilon = \left(\frac{R_{11}}{\varepsilon_0^2 \, g_{11}} \right)^{1/2},$$ (4.8)

and the g_{11} value obtained in Section 4.2, which has been modified from the measured value of $g_{11} = 0.17$ m^4 C^{-2} for the previous composition to $g_{11} = 0.257$ m^4 C^{-2} for the present one according to the composition dependence given by Buse et al. [84], a relative dielectric permittivity of $\varepsilon \approx 2000$ can be calculated and agrees well with the $\varepsilon = 2100$ measured directly.

In terms of modulation speed, we were limited by the availability of amplifiers capable of generating the modulation voltage in the 100 V range. We demonstrated electro-optic modulation at $f = 10$ MHz as shown in Fig. 4.12, but since the material family of potassium tantalate niobate has proven its applicability in the GHz range [13] in similar configurations, we have no reason to expect any fundamental limitation up to several GHz once the modulation voltage has been reduced by the methods described in the next section.

4.5 Discussion

The fundamental suitability of epitaxial KNTN thin films on KT substrates for electro-optical integrated waveguide devices has been demonstrated and shows promising properties like high lateral index contrasts, allowing small devices, while maintaining excellent material interfaces and good optical surfaces. The relative dielectric permittivity and Kerr coefficients rank among the highest of all materials reported so far and all the limitations described in Chapter 3 have successfully been addressed. However, to pave the way for real device use, two main restrictions have to be overcome: the half-wave voltage V_π has to be diminished and the propagation
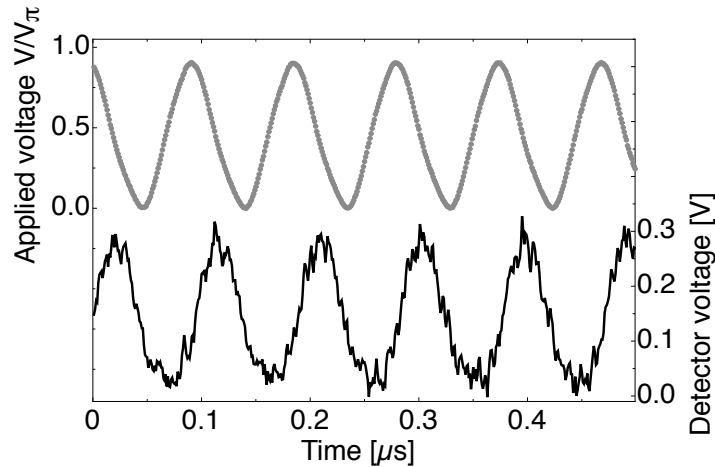
Figure 4.12: Electro-optic modulation at $f = 10$ MHz in potassium sodium niobate tantalate thin film ridge waveguide phase modulator. Upper curve shows voltage applied to the side electrodes in units of half-wave voltage, lower curve shows detected light intensity.

losses have to be reduced. We will first discuss one approach to address both issues simultaneously and then talk about additional measures individually. As stated in Sections 4.3 and 4.4, the propagation losses mainly stem from the etched side walls of the waveguide, while the top surface is of good optical quality, and the half-wave voltage is approximately 100 V due to the huge difference in the relative dielectric permittivity of the KNTN thin film ($\varepsilon \approx 2100$) and the KT substrate ($\varepsilon \approx 240$). Accordingly, we suggest a simple modification to the waveguide production process that will greatly improve both the loss and V_π values: instead of etching ridges the full height of the thin film, the etch depth will be reduced to $h = 1.4$ μm, and 2 μm of the KNTN thin film will remain as a pedestal beneath the ridge. Simulations performed in OlympIOs ensure the continued monomodality of the ridge waveguide. The effects will be twofold: first of all, the propagating mode has much less inter-action with the etched waveguide side walls, which reduces propagation losses and secondly, the electrodes now also reside on the thin film material which increases the electric field strength inside the waveguide core area. To illustrate this effect, both geometries were modeled in Comsol Multiphysics. The result is shown in Fig. 4.13 and indicates that in case (b) with shallower ridge waveguides, the electric field component E_x is 7 times stronger than in the present case (a) for the same voltage applied to the electrodes. Conversely, to achieve the same phase shift, the half wave voltage V_π drops from 100 V to about 14 V. When also taking into account the electrode length l, the figure of merit $V_\pi l$ of this suggested geometry is among the lowest values reported so far [13].

Other possible methods to reduce V_π: (1) increasing the length of the waveguide and the electrodes, which may potentially increase device size, (2) biasing the mod-ulator with a DC voltage, since V_π decreases with a DC bias due to the quadratic electro-optic effect as demonstrated in Fig. 4.11, or (3) changing the material compo-sition to shift the phase transition temperature closer to the operation temperature.
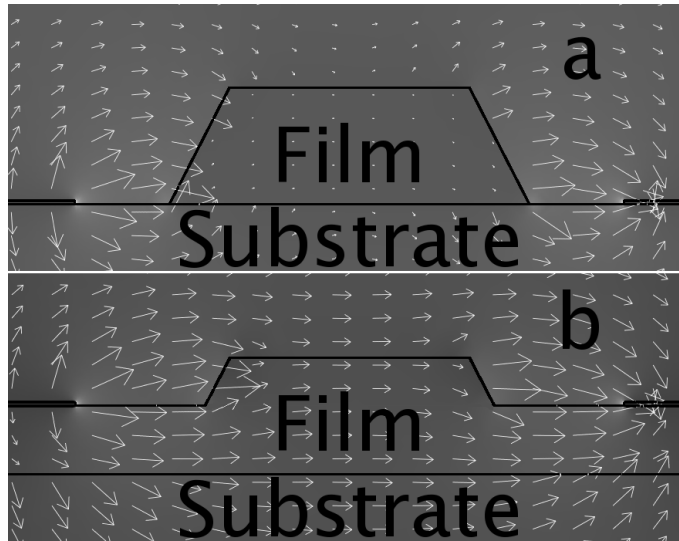
Figure 4.13: Existing (a) and suggested (b) waveguide geometries to significantly reduce half-wave voltage in potassium sodium niobate tantalate thin film ridge waveguide phase modulator. Placing the electrodes on the thin film instead of on the substrate increases the electric field in the waveguide core by a factor of seven.

In regards to reducing the losses, the etching process itself can be further optimized, or the waveguide could be covered with a thin layer, SiO_2 or Si_3N_4 for example, to reduce the surface roughness, though it is difficult to estimate the amount of loss reduction that would be achievable by these means.

4.6 Conclusion

Electro-optic modulation in paraelectric epitaxially grown KNTN thin films on KT substrates at $\lambda = 1550$ nm has been reported here for the first time to the best of our knowledge, exploiting a thin film Kerr coefficient of $(8.2 \pm 1.1) \times 10^{-17}$ m^2/V^2. While rather simple measures will allow for a decrease in both propagation losses and the half-wave voltage of the demonstrated ridge waveguide phase modulator, this achievement already constitutes an important step towards more sophisticated integrated optics devices, such as Mach-Zehnder modulators or cross-switches, that utilize the outstanding dielectric and electro-optic properties of the KTN material family.

Chapter 5

Applications

In the previous two chapters, the promising features of electro-optic KNTN thin films have been demonstrated, and with the ridge waveguide phase modulator, a proof of concept device has been produced that shows the potential of KNTN thin film optics. In this chapter we will now talk about the applicability of these films to future real world devices. While we have already mentioned the generation of higher harmonics in ridge waveguides (see Chapter 2), the focus in this section will be on two specific devices: the Mach-Zehnder interferometer and the microring resonator.

The main drawback of the waveguide phase modulator presented in Chapter 4 is that it's not an *integrated optics* device. In order for the modulator to work, we need the 45 ° polarizer at the input facet, exciting both the TE and TM mode inside the waveguide, and the 135 ° analyzer at the output, converting the electro-optically induced phase shift into an amplitude modulation. These two optical elements cannot be integrated into the optical circuit built from the KNTN thin film and prevent the modulator from being fiber-coupled to the rest of the setup, an absolute must for real world applications. The two device designs presented in this chapter need no external optical elements (other than the light source and the detector of course) and therefore could be sealed and packaged for industrial use.

5.1   Mach-Zehnder interferometer

5.1.1   Operation principle

The Mach-Zehnder interferometer (MZI, see Fig. 5.1 for a schematic drawing) is a phase modulator similar to the one presented in Chapter 4, but unlike the latter performs the action of converting the phase shift into an amplitude variation on-chip, that is without external optical elements. The incoming light (either TE or TM polarized, and even polarization-independent operation has been demonstrated [85]) is split into two halves in a first 3 dB coupler. The two fractions then propagate independently in the two parallel arms of the interferometer where they are subject to the electro-optic effect generated by the electric field applied to the electrodes adjacent to the waveguides. It is important to note that the electric field points in opposite directions across the two waveguides, which creates a complementary refractive index change in the two arms and effectively doubles the induced phase
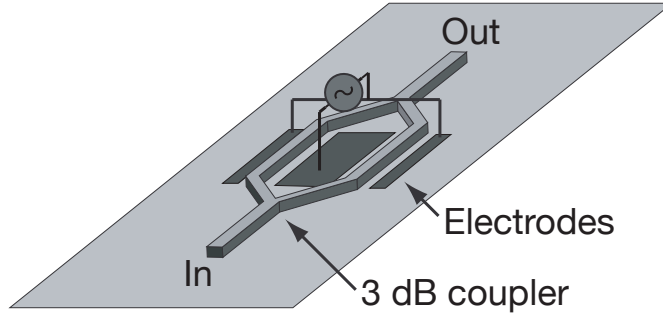
Figure 5.1: Schematic drawing of an integrated Mach-Zehnder modulator.

shift. In a second 3 dB coupler, the two arms are then recombined. It is here that the actual interference takes place, as depending on the relative phase shift of the two modes, they either combine constructively ($\Delta\varphi = n \cdot 2\pi, \quad n \in \mathbb{N}$) or cancel each other ($\Delta\varphi = n \cdot \pi, \quad n \in \mathbb{N}$). If the MZI is well balanced (both arms share the same optical properties), the optical power at the output is given by

$$P_{\text{out}} = P_{\text{max}} \cos^2\left(\frac{\Delta\varphi}{2}\right), \tag{5.1}$$

where the phase shift $\Delta\varphi$ can be expressed by

$$\Delta\varphi_{\text{lin}} = -\frac{2\pi n^3 L\Gamma}{\lambda} rE \tag{5.2}$$

if induced by the linear electro-optic effect and by

$$\Delta\varphi_{\text{qua}} = -\frac{2\pi n^3 L\Gamma}{\lambda} RE^2 \tag{5.3}$$

for the Kerr effect and L is the electrode length, Γ is a factor specifying the attenuation of the electric field inside the waveguide ($E_x = \Gamma \cdot V/d$), λ is the wavelength of the light, and E is the strength of the electric field created by the electrodes. MZIs are the standard modulators in today's telecom industry and have been produced in a variety of materials like lithium niobate [86], silicon-on-insulator (SOI) [87] or polymers [88].

5.1.2 Mach-Zehnder interferometer in $K_{1-y}Na_yTa_{1-x}Nb_xO_3$ thin films

Due to a lack of a sufficient number of thin film samples, a KNTN Mach-Zehnder interferometer could unfortunately not be produced in the course of this thesis. Contrary to the phase modulator presented in Chapter 4, a MZI requires a photolithography mask specifically designed for the optical parameters of the thin film/substrate complex. The work described in Chapters 3 and 4 yields these parameters and we can therefore propose an integrated electro-optic KNTN thin film Mach-Zehnder modulator with an unbiased halfwave voltage of $V_\pi = 10$ V and a total device length of $l < 10$ mm. The design is based on the waveguide geometry proposed in
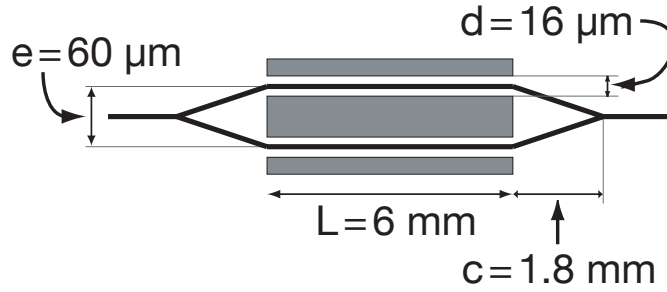
Figure 5.2: Layout of proposed KNTN Mach-Zehnder modulator.

Fig. 4.13 (b) and is shown in Fig. 5.2 (not to scale). The 3 dB couplers are each $c = 1.8$ mm long and lead to a waveguide separation of $e = 60$ μm. Between the two arms, a central electrode of dimensions $L = 6$ mm by $w = 50$ μm is deposited, separated from the two side electrodes by $d = 16$ μm.

From equation (5.3) we can deduce the halfwave voltage of this modulator to be given by

$$V_\pi = \sqrt{\frac{\lambda d^2}{2n^3 LR\Gamma}}. \tag{5.4}$$

Using the parameters $\Gamma = 1/3$ (from the simulation that produced Fig. 4.13), $\lambda = 1.5$ μm, $d = 16$ μm, $n = 2.18$, and $R = 8.2 \times 10^{-17}$ m^2/V^2 (both from Chapter 4), we get V_π as a function of the electrode length L as shown in Fig. 5.3, indicating device operation at $V_\pi = 10$ V for an interaction length of $L = 6$ mm.
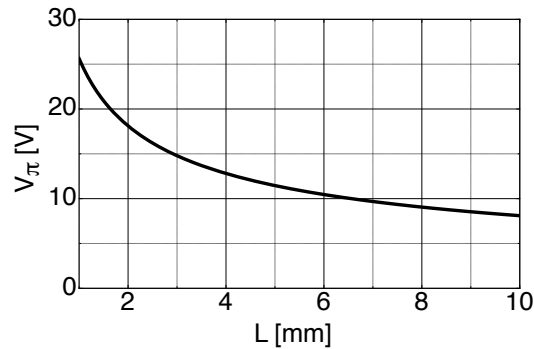
Figure 5.3: Halfwave voltage as a function of electrode length for proposed integrated KNTN Mach-Zehnder modulator.

Additional methods to further decrease the halfwave voltage V_π are discussed in Section 4.5 and can be directly applied to the Mach-Zehnder design proposed here.

5.2 Microring Resonator

For the last two decades, microring resonators have been one of the hottest topics in the integrated optics community due to their outstanding features and wide ap-

plicability. Our group is very active in this field and has recently demonstrated a novel polymer microring processing method [44] and the first electro-optic thin film lithium niobate ring resonator [43].

5.2.1 Operation principle

A microring resonator is a resonant device consisting of a circular or oval cavity and two (sometimes just one) port waveguides, coupled to the ring either vertically or laterally. The basic scheme is shown in Fig. 5.4 and indicates the main design parameters: the radius R of the ring and the coupling constants κ_1 and κ_2 between resonator and port waveguides, mainly determined by their spacing. When light from the input port reaches the coupling region, a fraction κ_1 of the amplitude is transferred to the ring resonator and starts circling inside the cavity. For each
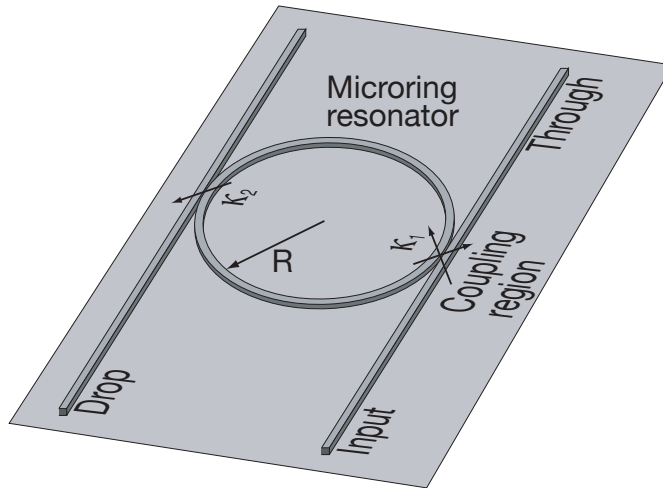
Figure 5.4: Schematic drawing of a microring resonator with radius R and two port waveguides with coupling coefficients κ_1 and κ_2 to the resonator.

round-trip inside the ring, the propagating optical power experiences a phase shift of $\varphi = \frac{2\pi}{\lambda} N L$, where N is the effective mode index and the circumference L is given by $L = 2\pi R$, and a round-trip attenuation factor of

$$\sigma = \exp\left(-\frac{\ln 10}{20} \cdot \alpha L\right), \tag{5.5}$$

where α is the propagation loss given in dB/cm. If the *resonance condition*

$$\varphi = 2\pi n, \quad n \in \mathbb{N} \tag{5.6}$$

is met, that is if an integer number of wavelengths "fit" into the resonator, the power at the *drop* port is maximum while the *through* port shows a minimum. Since φ depends on the wavelength λ, the optical power at the *through* port as a function of

λ is then given by [42]

$$T(\lambda) = \frac{(\sigma' - \tau)^2 + 4\sigma'\tau \sin^2\left(\frac{2\pi^2}{\lambda}NR\right)}{(1 - \sigma'\tau)^2 + 4\sigma'\tau \sin^2\left(\frac{2\pi^2}{\lambda}NR\right)}, \tag{5.7}$$

where σ' combines the round-trip loss σ and the drop losses induced by κ_2, and τ is the amplitude fraction transmitted through the coupling region: $\tau = \sqrt{1 - \kappa^2}$. An example of the simulated wavelength response of a microring resonator with $R = 100$ μm, $\alpha = 12$ dB/cm, $N = 2.2$ and $\kappa_1 = 0.4$ is shown in Fig. 5.5. Key
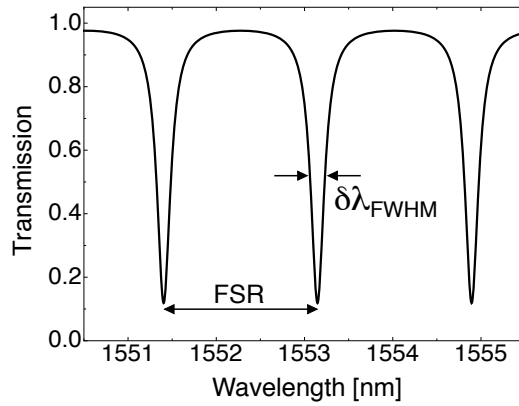

Figure 5.5: Calculated wavelength response of a microring resonator with $R = 100$ μm, $\alpha = 12$ dB/cm, $N = 2.2$ and $\kappa_1 = 0.4$.

parameters of a microring resonator are the *free spectral range* (FSR), which is given by the distance between two adjacent resonances, and the *spectral width* $\delta\lambda_{\text{FWHM}}$ which indicates how "sharp" the resonances are. As is usual for resonators, we define the *finesse* as $\mathcal{F} = \text{FSR}/\delta\lambda_{\text{FWHM}}$ and the *quality factor* as $Q = \lambda/\delta\lambda_{\text{FWHM}}$. Both parameters are indicators for the performance of the resonator – usually the higher the better. It is obvious that a ring resonator with a sufficiently high Q makes for an ideal modulator candidate if the effective mode index N can be varied by the electro-optic effect. Further details on theory, design and production of ring resonators can be found in [42, 89, 90].

It is also instructive to take a look at the calculated intensity distribution inside the ring resonator in and off resonance, shown in Fig. 5.6. Note that in the resonance case, the light intensity inside the ring can be several times higher than the input intensity. It is this resonant field enhancement that makes microring resonators so attractive for electro-optic and sensor applications, since very high field effects can be achieved with moderate input powers.

5.2.2 Microring resonators in $K_{1-y}Na_yTa_{1-x}Nb_xO_3$ thin films

From the beginning of the group's activity in microring resonators, KNTN has been recognized as one of the most auspicious materials to be used for the production of such devices, owing to its good optical quality thin films, the large electro-optic coefficients and the high refractive index which provides a good lateral confinement

Off-resonance   In resonance
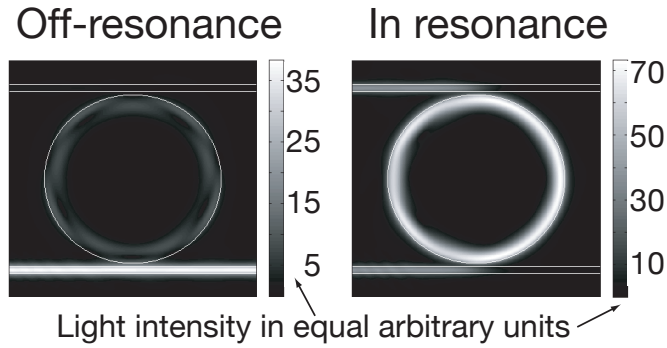

Light intensity in equal arbitrary units

Figure 5.6: Simulated intensity distribution in a microring resonator off-resonance (left) and in resonance (right). Note the field enhancement in the resonant cavity.

for rings of small radius. Quite some effort has been put into the simulation and design of KNTN thin film microring resonators, but unfortunately with the present technology of growing the KNTN films on KT substrates, the production of working microrings will not be possible, as my own simulations have shown and is reasoned in detail in a recent Ph.D. thesis [42]. The problem is the low index contrast between the KT substrate and the KNTN film material. As soon as the waveguide is not straight, even a large-radius bend "squeezes" the light out of the ridge waveguide and into the substrate. Several configurations like a KT pedestal beneath the waveguide have been simulated, but to no avail. Unless the KNTN film is grown on a substrate with lower refractive index, a successful confinement of the mode in bent waveguides will not be possible. In this case, the process of matching the lattice parameters has to be repeated and it is very questionable whether an equally good substrate-film interface could be achieved. The index of the KNTN film material cannot be increased significantly since it already is almost on par with the bulk value (Fig. 4.7). A typical simulation of a ring with a large radius of $R = 300\ \mu$m is depicted in Fig. 5.7 and clearly shows the mode squeezing, leading to prohibitive loss values of hundreds of dB/cm.
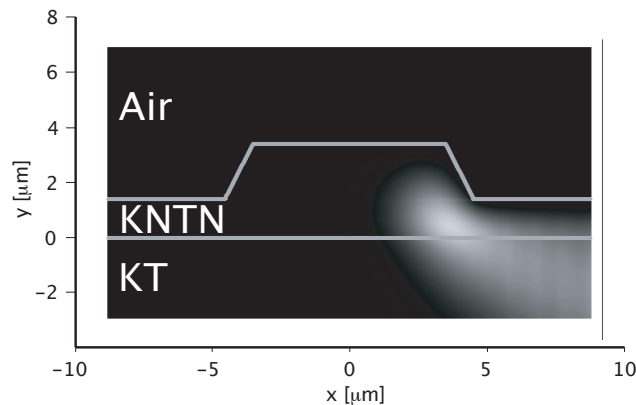

Figure 5.7: Insufficient mode confinement in KNTN thin film microring resonator with radius $R = 300\ \mu$m.

Chapter 6

Conclusion and outlook

As the previous chapters have shown, potassium sodium tantalate niobate (KNTN) is an extremely appealing material for integrated electro-optic waveguide devices. Its remarkably high dielectric and electro-optic coefficients and particularly the temperature-tunability of the phase transition achievable by varying the Nb:Ta ratio provide an application flexibility that few, if any, other materials possess. After the technological challenges of growing epitaxial KNTN thin films of optical quality on potassium tantalate (KT) substrates have been overcome, the successful demonstration of electro-optic phase modulation in monomodal ridge KNTN waveguides marks an important step towards the adoption of KNTN thin films in more advanced electro-optic devices. While the limited index contrast between KT substrates and KNTN thin films may impede their use in some special applications like microring resonators, other devices benefit from the superior interface quality between substrate and film – finally, a high index contrast is always evidence for a pronounced incompatibility between the two materials involved that renders a seamless interface unlikely.

In various sections of the previous chapters we have already touched on the subject of possible actions to further maximize the material parameters of the KNTN thin films and to optimize device performance. Summarizing these ideas, we now compile a list of recommendations of the directions in which to conduct further research.

- We have seen in Chapter 4 that the present thin film material composition of $K_{0.95}Na_{0.05}Ta_{0.71}Nb_{0.29}O_3$ exhibits the phase transition $\Delta T \approx 30\,°C$ below room temperature. By adjusting the Nb:Ta ratio to be close to 0.4:0.6, the Curie point could be shifted even closer to room temperature which would increase the Kerr coefficient threefold (Fig. 4.2 and equation (4.2)).

- As detailed in Section 4.5, simple modifications to the waveguide design can tremendously increase the strength of the applied electric field inside the waveguide core, by at least a factor of seven. Together with the change in material composition described above, this would cut down the halfwave voltage of a phase modulator or a Mach-Zehnder interferometer to one twelfth of the current value.

- In Section 2.4.2 we motivated the use of paraelectric films by the need for polarization-insensitive waveguides and the difficulty to permanently pole ferroelectric thin films into a monodomain state. Integrated optics devices like the Mach-Zehnder modulator proposed in Chapter 5 don't rely on the concurrent propagation of two polarizations which eliminates one obstacle towards the use of ferroelectric KNTN thin films with large Pockels coefficients.

- Poling problems, the other challenge inhibiting ferroelectric KNTN thin films, could probably be overcome by taking advantage of the conducting barium-doped KT substrates mentioned in Section 2.4.4. Since the lattice matching between the substrates and the thin films is so extraordinarily good in our samples and monodomain poling is definitely possible for bulk crystals, maybe the stress minimization constraint described by Gopalan [57] and Pertsev [58] for substrate/thin film combinations with a much larger lattice mismatch is not strictly valid in our bulk-like material and single-domain ferroelectric KNTN thin films could be achieved.

Summing it all up, we are confident that the exceptional properties of KNTN thin films justify a prominent place of this material complex in the integrated optics industry and we hope that this Ph.D. thesis might contribute a bit to the advocacy for this interesting material.

Appendix A

Electro-optic behavior of lithium niobate at cryogenic temperatures †

The unclamped relative permittivity, ε_{33}^T, and the Pockels coefficient, r_{33}^T, of congruent lithium niobate at a frequency $f = 5760$ Hz have been determined at low temperatures (7 K $< T <$ 300 K). A He cryostat setup mounted to one arm of an electronically phase-stabilized Michelson interferometer was utilized for the measurement of r_{33}^T . A continuous decrease in both parameters was observed as $T \to 0$ K with limiting values of $\varepsilon_{33}^T \approx 25.4 \pm 0.1$ and $r_{33}^T \approx 24 \pm 0.7$ pm/V, respectively.

A.1   Introduction

Lithium niobate (LN) is an important material for many electro-optical devices in today's telecom industry and for this reason has been intensely studied in recent decades. A wealth of mechanical, dielectric [92, 93, 94], optical, and electro-optical [95, 96, 97] data for LN has been compiled over the last several years and is readily available as, e.g., reviewed by Weis et al. [21], with the notable exception of electro-optic behavior at cryogenic temperatures. Yet the temperature dependence of the electro-optic coefficients is particularly interesting for theoretical as well as practical reasons. From a basic research point of view, Glass's discovery [98], which was later confirmed by Vieira [99, 100], of a local maximum around $T = 30$ K in the pyroelectric figure of merit p/C, where p is the pyroelectric coefficient and C is the specific heat, raised the question whether electro-optic coefficients would exhibit low-temperature anomalies, since both p and the electro-optic Pockels coefficients are related to the spontaneous polarization P_s. LN-based modulators have been suggested in areas as diverse as communication with superconducting circuits [101] or large particle detectors [102] and in addition, superconducting electrodes in LN modulators have been proposed [103]. However, studies have concentrated on actual device performance and the viability of these devices has been demonstrated by measuring the half-wave voltage, V_π, of packaged and fiber-coupled modulators upon cooling

---

†An abbreviated version of this chapter has been submitted to Optics Communications [91].

to cryogenic temperatures [104,105], while the basic material Pockels coefficient has not yet been measured at very low temperatures. To the best of our knowledge, we present the first direct measurement of the unclamped Pockels coefficient r_{33}^T as well as the unclamped relative permittivity ε_{33}^T of congruent lithium niobate over the temperature range of 7 K $< T <$ 300 K. The measurements were performed in a He cryostat incorporated into an electronically phase-stabilized Michelson interferometer (see below) at $\lambda = 632.8$ nm and with an HP 4192 impedance bridge, respectively. The measured r_{33}^T values are compared to literature values and the temperature dependence of the linear polarization-optic coefficient f_{33} is given.

A.2 Theory and experiment

As already noted in the introduction, a local maximum of p/C, where p is the pyroelectric coefficient and C is the specific heat, exists at approximately 30 K in lithium niobate. The term p is related to the spontaneous polarization P_s by

$$p = -\frac{\Delta P_s}{\Delta T},\tag{A.1}$$

which raises the question whether a related anomaly is present in the Pockels coefficient r_{33}^T, which depends on P_s via

$$r_{33}^T = \varepsilon_0 \left(\varepsilon_{33}^T - 1\right) f_{33},\tag{A.2}$$

where ε_0 is the vacuum permittivity and the linear polarization-optic coefficient f_{33} is given by

$$f_{33} = 2/3(g_{11} + 2g_{12} + 2g_{44})P_s\tag{A.3}$$

for crystals with a $3m$ point group symmetry like LN [26] and g_{ij} are the quadratic polarization-optic coefficients.

To elucidate this question, measurements of ε_{33}^T and r_{33}^T were performed on z-cut crystals of congruent lithium niobate in an evacuated (10^{-5} mbar) liquid helium cryostat from Cryo Industries at a frequency of $f = 5760$ Hz. This frequency was chosen in order to meet the following criteria: (i) it is above the cut-off frequency of the adaptive phase compensation circuit as described later in this paper, yet well below any mechanical resonance frequencies of the crystal, the lowest of which occurs at approximately 300 kHz. Furthermore, it is (ii) low enough to be detectable by the Stanford Research SR830 lock-in amplifier and (iii) sufficiently low so that high-frequency effects of the cabling and the test fixture can be neglected. The crystals were mounted on the cold head of the cryostat in an unclamped way. Electrical isolation with simultaneous good thermal coupling was achieved by separating the lower electrode from the cold head with a piece of an oxidized highly doped silicon wafer with 2 μm of silicon oxide on either side and the use of indium foil on all interfaces. The maximum temperature difference between the cold head and the crystal, which was mounted on the lower electrode by silver paint, was approximately 0.4 K with heating rates of 1 K/min. For the measurement of the unclamped relative permittivity, an HP 4192 impedance analyzer was connected to the top and bottom

electrodes of a 510 μm thick z-cut plate of LN in a 4-wire configuration with coax cabling. The evacuated cryostat was then cooled to 7 K and the complex impedance of the system was recorded upon heating the cryostat to 300 K, controlled by a Lakeshore 330 temperature controller. The relative permittivity of the LN plate was then calculated using corrections for the parasitic impedance of the cryostat setup and the thermal expansion data for LN published by Browder [106]. The unclamped Pockels coefficient r_{33}^T of a cuboid of congruent LN was measured by mounting the cryostat in one arm of a Michelson interferometer (for the theory of the interferometric measurement, see Haertle et al. [107]). A schematic of the setup is shown in Fig. A.1.
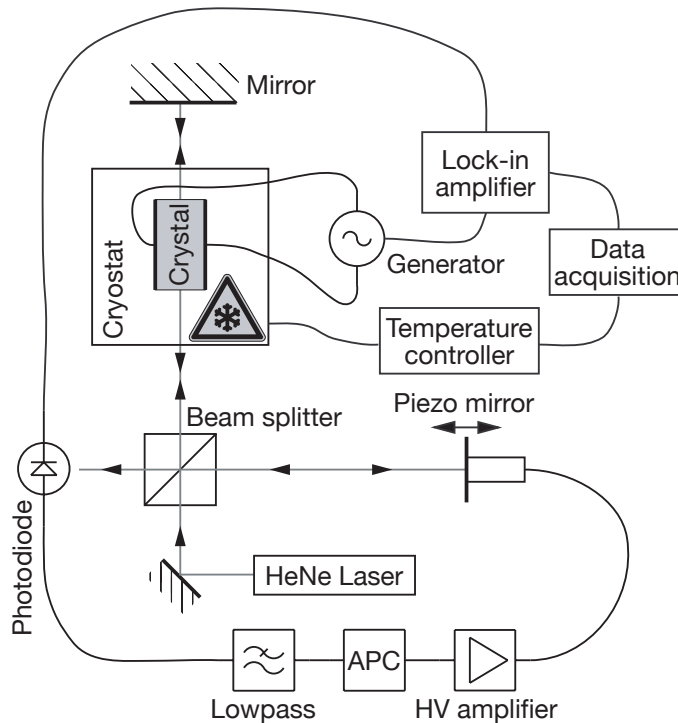

Figure A.1: Cryostatic interferometer setup used to measure the linear electro-optic coefficient r_{33}^T of lithium niobate bulk crystals. Low-frequency phase oscillations are compensated by an adaptive phase compensation.

When a sinusoidal voltage is applied to the electrodes of the LN crystal, the phase shift created by the electro-optic effect in the crystal causes an intensity modulation when the signal and the reference beam interfere. If the induced intensity modulation δI is small compared to the full intensity range $\Delta I = I_{max} - I_{min}$, r_{33}^T can be calculated from

$$r_{33}^T = \frac{d\lambda \delta I}{\pi L n^3 V_{app} \Delta I},$$
(A.4)

where $d = 4.16$ mm is the height of the crystal, $\lambda = 632.8$ nm is the laser wavelength, $L = 5.81$ mm is the length of the crystal in propagation direction, $n(T)$ is the temperature-dependent refractive index taken from Schlarb et al. [23] and V_{app}

is the amplitude of the applied modulation voltage. For each data point, the temperature was stabilized to ± 0.05 K for 10 min before multiple lock-in readings were recorded. The d and L values were corrected for thermal expansion. With decreasing temperature, a rapidly increasing low-frequency random phase noise (the origin of which could not be conclusively determined but which is believed to emanate from the material itself) made the fixation of the working point of the interferometer at $1/2(I_{max} + I_{min})$ unfeasible. This setback was addressed by introducing an adaptive phase compensation (APC) into the reference arm of the interferometer. The photodiode signal carrying the phase noise was sent through a lowpass filter with a cutoff frequency of approximately 200 Hz to a PI controller built around Burr-Brown INA118P and OPA27GP operational amplifiers. The compensation signal created by this APC was amplified and fed to a piezo-driven mirror, allowing for an elimination of the phase noise while maintaining full operation at modulation frequencies higher than the lowpass cut-off.

A.3   Results

Fig. A.2 shows the unclamped relative permittivity of congruent LN over the temperature range of 7 K $< T <$ 300 K at $f = 5760$ Hz. The room temperature value of $\varepsilon_{33}^T \approx 28.9$ agrees well with the data given by Weis et al. [21]. Within experimental error, the permittivity levels off at $\varepsilon_{33}^T \approx 25.4 \pm 0.1$ for $T \to 0$ K.
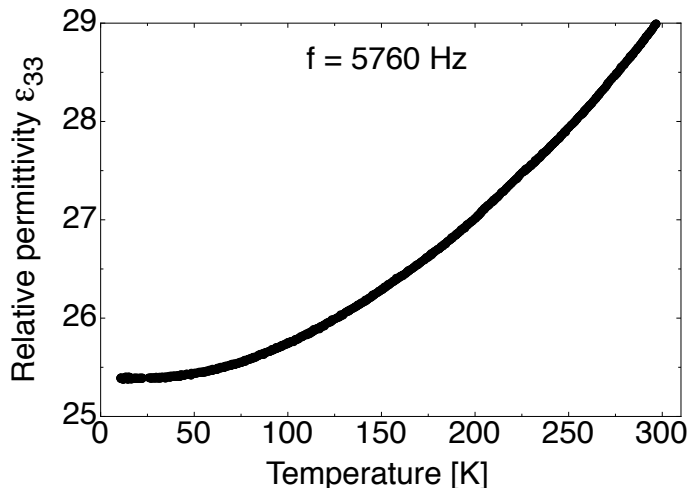
Figure A.2: Unclamped relative permittivity ε_{33}^T of congruent lithium niobate covering the temperature range of 7 K $< T <$ 300 K at $f = 5760$ Hz.

The temperature dependence of the unclamped Pockels coefficient r_{33}^T of congruent LN between 7 K and 300 K at $f = 5760$ Hz is presented in Fig. A.3. Once again the measured r_{33}^T values agree with those reported literature [21], but no maximum was observed at ~ 30 K within the given experimental precision. The temperature dependence much resembles that of the dielectric permittivity and a lower limit of $r_{33}^T \approx 24$ pm/V can be expected as $T \to 0$ K.
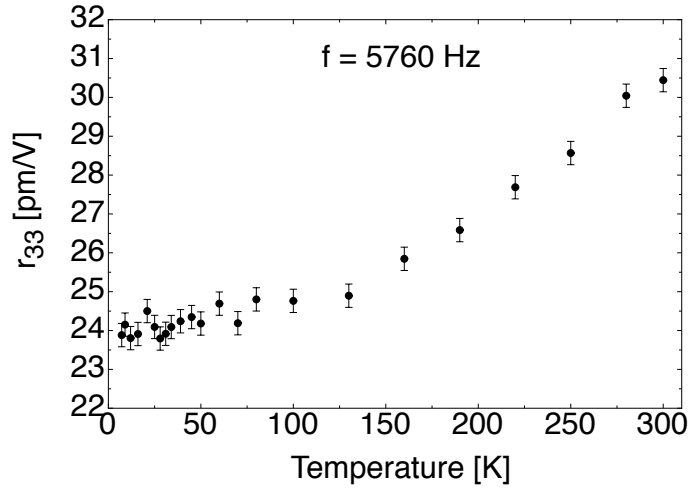
Figure A.3: Unclamped Pockels coefficient r_{33}^T of congruent lithium niobate covering the temperature range of 7 K $< T <$ 300 K at f = 5760 Hz and $\lambda = 632.8$ nm.

The linear polarization-optic coefficient f_{33} can be calculated by using the measured ε_{33}^T and r_{33}^T values according to equation (A.2). The results are shown in Fig. A.4 and exhibit a temperature dependence that can be understood from equation (A.3) and the temperature characteristics of P_s as measured by Glass [98] and Vieira [99]. In contrast to f_{33}, the quadratic polarization-optic coefficients g_{ij} are remarkably constant with temperature [76]. Using literature values of $g_{11} = 0.093$ m^{4}C^{-2}, $g_{12} = 0.025$ m^{4}C^{-2}, and $g_{44} = 0.064$ m^{4}C^{-2} (Wemple et al. [26]) for lithium niobate in combination with equation (A.3), a room temperature value of $f_{33} \approx 0.13$ m^2/C is obtained, agreeing well with our $f_{33} \approx 0.123 \pm 0.012$ m^2/C. The linear polarization-optic coefficient f_{33} decreases with decreasing temperature to reach $f_{33} \approx 0.112 \pm 0.0024$ m^2/C below 80 K.
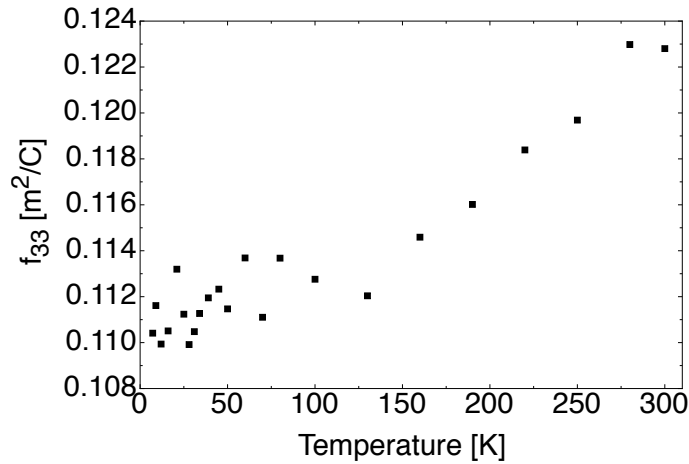

Figure A.4: Linear polarization-optic coefficient f_{33} of congruent lithium niobate at a wavelength $\lambda = 632.8$ nm, covering the temperature range of 7 K $< T <$ 300 K, calculated from Fig. A.2 and Fig. A.3 data.

A.4 Discussion

Our measurements of r_{33}^T show a 20 % decrease upon cooling the LN crystal from room temperature to 10 K. Morse [104] and McConaghy [105] report a $8 - 9$ percent increase in the half-wave voltage V_π of commercial LN Mach-Zehnder modulators over this temperature range at wavelengths of $0.8 - 1.3$ μm. V_π in these modulators is given by

$$V_\pi = \lambda s/(2n^3 r_{33} L \Gamma), \tag{A.5}$$

where s is the electrode spacing, L is the electrode length, and Γ is a field overlap factor. Of these parameters, only n varies with temperature, albeit not significantly. Hence, the increase in V_π is somewhat smaller than expected from the observed decrease in r_{33}.

A.5 Conclusion

The unclamped relative permittivity ε_{33}^T and the Pockels coefficient r_{33}^T of congruent lithium niobate have been measured between 7 K and room temperature for the first time to the best of our knowledge. Both parameters exhibit a continuous decrease and converge to steady values of $\varepsilon_{33}^T \approx 25.4 \pm 0.1$ and $r_{33}^T \approx 24 \pm 0.7$ pm/V, respectively below 50 K. The linear polarization-optic coefficient f_{33} has been shown to decrease almost linearly from room temperature to 100 K and then remains roughly constant down to 7 K.

Bibliography

[1] R. GUTMANN, 'Liquid phase epitaxy of para- and ferroelectric $KTa_{1-x}Nb_xO_3$', *Diss. ETH No. 10095* (1993)

[2] H. PIERHÖFER, 'Investigation of epitaxial ferroelectric $K_{1-y}Na_yTa_{1-x}Nb_xO_3$ on Ba doped $KTaO_3$ substrates', *Diss. ETH No. 13459* (1999)

[3] C. KITTEL, 'Introduction to Solid State Physics', *John Wiley and Sons* (1986)

[4] F. JONA AND G. SHIRANE, 'Ferroelectric Crystals', *Dover Publications* (1993)

[5] G. BURNS, 'Solid State Physics', *Academic Press, Inc.* (1990)

[6] M. E. LINES AND A. M. GLASS, 'Principals and Applications of Ferroelectrics and Related Materials', *Oxford University Press* (1977)

[7] T. ITOH, M. SASAURA, S. TOYODA, K. MANABE, K. NAKAMURA, AND K. FUJIURA, 'High-frequency response of electro-optic single crystal $KTa_xNb_{1-x}O_3$ in paraelectric phase', *2005 Quantum Electronics and Laser Science Conference (QELS) (IEEE Cat. No. 05CH37696)* (2005)

[8] Y. XU, 'Ferroelectric Materials and Their Applications', *North-Holland* (1991)

[9] S. STAMENKOVIC, N. M. PLAKIDA, V. L. AKSIENOV, AND T. SIKLOS, 'Unified Theory of Ferroelectric Phase-Transitions', *Physical Review B* **14**, 5080–5087 (1976)

[10] H. IWASAKI, 'Studies on System (1-x)NaNbO$_3$ xKTaO$_3$', *Journal of the Physical Society of Japan* **17**, 779– (1962)

[11] G. SHIRANE, R. NATHANS, AND MINKIEWI.VJ, 'Temperature Dependence of Soft Ferroelectric Mode in $KTaO_3$', *Physical Review* **157**, 396– (1967)

[12] J. H. BARRETT, 'Dielectric Constant in Perovskite Type Crystals', *Physical Review* **86**, 118–120 (1952)

[13] K. FUJIURA AND K. NAKAMURA, 'KTN optical waveguide devices with an extremely large electro-optic effect', in Y. SUN, S. S. JIAN, S. B. LEE, AND K. OKAMOTO, editors, *Passive Components and Fiber-Based Devices, Pts 1 and 2*, volume 5623 of *Proceedings of the Society of Photo-Optical Instrumentation Engineers (SPIE)*, pages 518–532 (2005), conference on Passive Components and Fiber-based Devices Nov 09-11, 2004 Beijing, China

[14] K. Yamanouchi, Y. Wagatsuma, H. Odagawa, and Y. Cho, 'Single crystal growth of $KNbO_3$ and application to surface acoustic wave devices', *Journal of the European Ceramic Society* **21**, 2791–2795 (2001)

[15] B. H. Hoerman, B. M. Nichols, and B. W. Wessels, 'The electro-optic properties of epitaxial $KTa_xNb_{1-x}O_3$ thin films', *Optics Communications* **219**, 377–382 (2003)

[16] M. Sasaura, T. Imai, H. Kohda, S. Tohno, M. Shimokozono, H. Fushimi, K. Fujiura, S. Toyoda, K. Enbutsu, A. Tate, K. Manabe, T. Matsuura, and T. Kurihara, 'TSSG pulling and LPE growth of $KTa_xNb_{1-x}O_3$ for optical waveguides', *Journal of Crystal Growth* **275**, e2099–e2103 (2005)

[17] J. Toulouse, X. M. Wang, L. A. Knauss, and L. A. Boatner, 'Dielectric Nonlinearity and Spontaneous Polarization of $KTa_{1-x}Nb_xO_3$ in the Diffuse Transition Range', *Physical Review B* **43**, 8297–8302 (1991)

[18] J. Lehman, G. Eppeldauer, J. A. Aust, and M. Racz, 'Domain-engineered pyroelectric radiometer', *Applied Optics* **38**, 7047–7055 (1999)

[19] J. H. Lehman, A. M. Radojevic, and R. M. Osgood, 'Domain-engineered thin-film $LiNbO_3$ pyroelectric-bicell optical detector', *IEEE Photonics Technology Letters* **13**, 851–853 (2001)

[20] S. L. Bravina, A. N. Morozovska, N. V. Morozovsky, and Y. A. Skryshevsky, 'Low-temperature pyroelectric phenomena in lithium niobate single crystals', *Ferroelectrics* **298**, 31–42 (2004)

[21] R. S. Weis and T. K. Gaylord, 'Lithium-Niobate - Summary of Physical-Properties and Crystal-Structure', *Applied Physics A-Materials Science & Processing* **37**, 191–203 (1985)

[22] K. K. Wong, 'Properties of Lithium Niobate', *INSPEC, Inc.* (2002)

[23] U. Schlarb and K. Betzler, 'Refractive-Indexes of Lithium-Niobate as a Function of Temperature, Wavelength, and Composition - a Generalized Fit', *Physical Review B* **48**, 15613–15620 (1993)

[24] P. F. Bordui, R. G. Norwood, D. H. Jundt, and M. M. Fejer, 'Preparation and Characterization of Off-Congruent Lithium-Niobate Crystals', *Journal of Applied Physics* **71**, 875–879 (1992)

[25] A. Yariv and P. Yeh, 'Optical waves in crystal: propagation and control of laser radiation', *J. Wiley & Sons* (1983)

[26] S. H. Wemple, M. DiDomenico, and I. Camlibel, 'Relationship between Linear and Quadratic Electro-Optic Coefficients in $LiNbO_3$, $LiTaO_3$ and Other Oxygen-Octahedra Ferroelectrics Based on Direct Measurement of Spontaneous Polarization', *Applied Physics Letters* **12**, 209–211 (1968)

[27] P. Bernasconi, M. Zgonik, and P. Günter, 'Temperature-Dependence and Dispersion of Electrooptic and Elasto-Optic Effect in Perovskite Crystals', *Journal of Applied Physics* **78**, 2651–2658 (1995)

[28] C. Bosshard, 'Nonlinear Optics', *Lecture notes, ETH Zurich* (1997)

[29] C. Herzog, S. Aravazhi, A. Guarino, A. Schneider, G. Poberaj, and P. Günter, 'Epitaxial $K_{1-x}Na_xTa_{0.66}Nb_{0.34}O_3$ thin films for optical waveguiding applications', *Journal of the Optical Society of America B* **24**, 829–832 (2007)

[30] M. Ingold and P. Günter, 'Linear Longitudinal Electro-Optic Effect in Oxygen Octahedra Ferroelectrics', *Ferroelectrics* **94**, 117–130 (1989)

[31] F. S. Chen, J. E. Geusic, S. K. Kurtz, J. G. Skinner, and S. H. Wemple, 'Light Modulation and Beam Deflection with Potassium Tantalate-Niobate Crystals', *Journal of Applied Physics* **37**, 388 (1966)

[32] E. Yablonovitch, 'Inhibited Spontaneous Emission in Solid-State Physics and Electronics', *Physical Review Letters* **58**, 2059–2062 (1987)

[33] *http://www.cudos.org.au/cudos/research/ultracompact_alloptical_switch.php*

[34] S. A. Maier, 'Plasmonics: Fundamentals and Applications', *Springer* (2007)

[35] L. Mutter, A. Guarino, M. Jazbinšek, M. Zgonik, P. Günter, and M. Dobeli, 'Ion implanted optical waveguides in nonlinear optical organic crystal', *Optics Express* **15**, 629–638 (2007)

[36] J. A. Harrington, 'A Review of IR Transmitting, Hollow Waveguides', *Fiber and Integrated Optics* **19**, 211–217 (2000)

[37] S. K. Y. Tang, B. T. Mayers, D. V. Vezenov, and G. M. Whitesides, 'Optical waveguiding using thermal gradients across homogeneous liquids in microfluidic channels', *Applied Physics Letters* **88** (2006)

[38] R. J. Mears, L. Reekie, I. M. Jauncey, and D. N. Payne, 'Low-Noise Erbium-Doped Fiber Amplifier Operating at 1.54 μm', *Electronics Letters* **23**, 1026–1028 (1987)

[39] C. A. Armiento, M. Tabasky, C. Jagannath, T. W. Fitzgerald, C. L. Shieh, V. Barry, M. Rothman, A. Negri, P. O. Haugsjaa, and H. F. Lockwood, 'Passive Coupling of InGaAsP/InP Laser Array and Singlemode Fibers Using Silicon Waferboard', *Electronics Letters* **27**, 1109–1111 (1991)

[40] *http://ronja.twibright.com/*

[41] A. Guarino, M. Jazbinšek, C. Herzog, R. Degl'Innocenti, G. Poberaj, and P. Günter, 'Optical waveguides in $Sn_2P_2S_6$ by low fluence MeV He+ ion implantation', *Optics Express* **14**, 2344–2358 (2006)

[42] A. GUARINO, 'Electro-optic microring resonators in inorganic crystals for photonic applications', *Diss. ETH No. 17029* (2007)

[43] A. GUARINO, G. POBERAJ, D. REZZONICO, R. DEGL'INNOCENTI, AND P. GÜNTER, 'Electro-optically tunable microring resonators in lithium niobate', *accepted for publication in Nature Photonics* (2007)

[44] D. REZZONICO, A. GUARINO, C. HERZOG, M. JAZBINŠEK, AND P. GÜNTER, 'High-finesse laterally coupled organic-inorganic hybrid polymer microring resonators for VLSI photonics', *IEEE Photonics Technology Letters* **18**, 865–867 (2006)

[45] H. ADACHI, T. KAWAGUCHI, K. SETSUNE, K. OHJI, AND K. WASA, 'Electrooptic Effects of (Pb, La)(Zr, Ti)O_3 Thin-Films Prepared by Rf Planar Magnetron Sputtering', *Applied Physics Letters* **42**, 867–868 (1983)

[46] R. C. ALFERNESS, 'Guided-Wave Devices for Optical Communication', *IEEE Journal of Quantum Electronics* **17**, 946–959 (1981)

[47] D. M. GILL, B. A. BLOCK, C. W. CONRAD, B. W. WESSELS, AND S. T. HO, 'Thin film channel waveguides fabricated in metalorganic chemical vapor deposition grown BaTiO_3 on MgO', *Applied Physics Letters* **69**, 2968–2970 (1996)

[48] V. GOPALAN AND R. RAJ, 'Domain structure and phase transitions in epitaxial KNbO_3 thin films studied by in situ second harmonic generation measurements', *Applied Physics Letters* **68**, 1323–1325 (1996)

[49] D. K. FORK, F. ARMANI-LEPLINGARD, AND J. J. KINGSTON, 'Application of electroceramic thin films to optical waveguide devices', *MRS Bulletin* **21**, 53–58 (1996)

[50] R. A. MCKEE, F. J. WALKER, J. R. CONNER, AND R. RAJ, 'BaSi$_2$ and Thin-Film Alkaline-Earth Silicides on Silicon', *Applied Physics Letters* **63**, 2818–2820 (1993)

[51] F. J. WALKER AND R. A. MCKEE, 'Thin-film perovskites-ferroelectric materials for integrated optics', *Nanostructured Materials* **7**, 221–227 (1996)

[52] *http://www.c2v.nl/products/software/olympios-software.shtml*

[53] *http://femlab.com/products/multiphysics/*

[54] S. TOYODA, K. FUJIURA, M. SASAURA, K. ENBUTSU, A. TATE, M. SHIMOKOZONO, H. FUSHIMI, T. IMAI, K. MANABE, I. MATSUURA, I. KURIHARA, S. C. J. LEE, AND H. DE WAARDT, 'KTN-crystal-waveguide-based electro-optic phase modulator with high performance index', *Electronics Letters* **40**, 830–831 (2004)

[55] M. Ohashi, K. Shiraki, and K. Tajima, 'Optical Loss Property of Silica-Based Single-Mode Fibers', *Journal of Lightwave Technology* **10**, 539–543 (1992)

[56] A. M. Zheltikov, 'Non λ^{-4} wavelength dependence of Rayleigh-scattering loss in waveguides', *Laser Physics* **16**, 960–964 (2006)

[57] V. Gopalan and R. Raj, 'Electric field induced domain rearrangement in potassium niobate thin films studied by in situ second harmonic generation measurements', *Journal of Applied Physics* **81**, 865–875 (1997)

[58] N. A. Pertsev and V. G. Koukhar, 'Polarization instability in polydomain ferroelectric epitaxial thin films and the formation of heterophase structures', *Physical Review Letters* **84**, 3722–3725 (2000)

[59] D. M. Gill, C. W. Conrad, G. Ford, B. W. Wessels, and S. T. Ho, 'Thin-film channel waveguide electro-optic modulator in epitaxial BaTiO$_3$', *Applied Physics Letters* **71**, 1783–1785 (1997)

[60] B. H. Hoerman, B. M. Nichols, M. J. Nystrom, and B. W. Wessels, 'Dynamic response of the electro-optic effect in epitaxial KNbO$_3$', *Applied Physics Letters* **75**, 2707–2709 (1999)

[61] D. Fluck and P. Günter, 'Second-harmonic generation in potassium niobate waveguides', *IEEE Journal of Selected Topics in Quantum Electronics* **6**, 122–131 (2000)

[62] T. Kawaguchi, K. Mizuuchi, K. Yamamoto, T. Yoshino, M. Imaeda, and T. Fukuda, 'Fabrication of thin-film waveguide QPM-SHG devices by domain-inverted liquid-phase epitaxy', *Journal of Crystal Growth* **191**, 125–129 (1998)

[63] J. P. Ansermet, D. Rytz, A. Chatelain, U. T. Hochli, and H. E. Weibel, 'Surface-Layer in Ferroelectric KTa$_{1-x}$Nb$_x$O$_3$', *Journal of Physics C-Solid State Physics* **14**, 4541–4551 (1981)

[64] P. Rabiei and W. H. Steier, 'Lithium niobate ridge waveguides and modulators fabricated using smart guide', *Applied Physics Letters* **86** (2005)

[65] Y. Q. Shi, C. Zhang, H. Zhang, J. H. Bechtel, L. R. Dalton, B. H. Robinson, and W. H. Steier, 'Low (sub-1-volt) halfwave voltage polymeric electro-optic modulators achieved by controlling chromophore shape', *Science* **288**, 119–122 (2000)

[66] A. Gumennik, A. J. Agranat, I. Shachar, and M. Hass, 'Thermal stability of a slab waveguide implemented by alpha particles implantation in potassium lithium tantalate niobate', *Applied Physics Letters* **87** (2005)

[67] Q. F. Xu, B. Schmidt, S. Pradhan, and M. Lipson, 'Micrometre-scale silicon electro-optic modulator', *Nature* **435**, 325–327 (2005)

[68] B. M. Nichols, B. H. Hoerman, J. H. Hwang, T. O. Mason, and B. W. Wessels, 'Phase stability of epitaxial $KTa_xNb_{1-x}O_3$ thin films deposited by metalorganic chemical vapor deposition', *Journal of Materials Research* **18**, 106–110 (2003)

[69] S. Toyoda, K. Fujiura, M. Sasaura, K. Enbutsu, A. Tate, M. Shimokozono, H. Fushimi, T. Imai, K. Manabe, T. Matsuura, and T. Kurihara, 'Low-driving-voltage electro-optic modulator with novel $KTa_{1-x}Nb_xO_3$ crystal waveguides', *Japanese Journal of Applied Physics Part 1-Regular Papers Short Notes & Review Papers* **43**, 5862–5866 (2004)

[70] K. Morishita, 'Index Profiling of 3-Dimensional Optical Wave-Guides by the Propagation-Mode near-Field Method', *Journal of Lightwave Technology* **4**, 1120–1124 (1986)

[71] G. L. Yip, P. C. Noutsios, and L. Chen, 'Improved propagation-mode near-field method for refractive-index profiling of optical waveguides', *Applied Optics* **35**, 2060–2068 (1996)

[72] R. Gutmann, J. Hulliger, and H. Wüest, 'Growth of Paraelectric and Ferroelectric Epitaxial Layers of $KTa_{1-x}Nb_xO_3$ by Liquid-Phase Epitaxy', *Ferroelectrics* **134**, 291–296 (1992)

[73] S. Aravazhi, A. Tapponnier, D. Gunther, and P. Günter, 'Growth and characterization of barium-doped potassium tantalate crystals', *Journal of Crystal Growth* **282**, 66–71 (2005)

[74] A. Schneider, F. Brunner, and P. Günter, 'Determination of the refractive index over a wide wavelength range through time-delay measurements of femtosecond pulses', *Optics Communications* **275**, 354–358 (2007)

[75] B. H. Hoerman, G. M. Ford, L. D. Kaufmann, and B. W. Wessels, 'Dielectric properties of epitaxial $BaTiO_3$ thin films', *Applied Physics Letters* **73**, 2248–2250 (1998)

[76] J. E. Geusic, S. K. Kurtz, L. G. Vanuitert, and S. H. Wemple, 'Electro-Optic Properties of Some ABO_3 Perovskites in Paraelectric Phase', *Applied Physics Letters* **4**, 141 (1964)

[77] C. Herzog, S. Reidt, G. Poberaj, and P. Günter, 'Electro-optic phase modulation in ridge waveguides of epitaxial $K_{0.95}Na_{0.05}Ta_{0.71}Nb_{0.29}O_3$ thin films', *Optics Express* **15**, 7642–7652 (2007)

[78] S. Triebwasser, 'Study of Ferroelectric Transitions of Solid-Solution Single Crystals of $KNbO_3$-$KTaO_3$', *Physical Review* **114**, 63–70 (1959)

[79] R. Gutmann, J. Hulliger, and E. Reusser, 'Liquid-Phase Epitaxy of Lattice-Matched $KTa_{1-x}Nb_xO_3$ Grown on $KTaO_3$ Substrate', *Journal of Crystal Growth* **126**, 578–588 (1993)

[80] H. PIERHÖFER, Z. SITAR, F. GITMANS, H. WÜEST, AND P. GÜNTER, 'New semiconducting substrate for heteroepitaxial growth of $K_{1-y}Na_yTa_{1-x}Nb_xO_3$', *Ferroelectrics* **201**, 269–275 (1997)

[81] L. A. KNAUSS, K. S. HARSHAVARDHAN, H. M. CHRISTEN, H. Y. ZHANG, X. H. HE, Y. H. SHIH, K. S. GRABOWSKI, AND D. L. KNIES, 'Growth of nonlinear optical thin films of $KTa_{1-x}Nb_xO_3$ on GaAs by pulsed laser deposition for integrated optics', *Applied Physics Letters* **73**, 3806–3808 (1998)

[82] K. NAKAMURA, J. MIYAZU, M. SASAURA, AND K. FUJIURA, 'Wide-angle, low-voltage electro-optic beam deflection based on space-charge-controlled mode of electrical conduction in $KTa_{1-x}Nb_xO_3$', *Applied Physics Letters* **89** (2006)

[83] H. Y. ZHANG, X. H. HE, Y. H. SHIH, K. S. HARSHAVARDHAN, AND L. A. KNAUSS, 'Optical and nonlinear optical study of $KTa_{0.52}Nb_{0.48}O_3$ epitaxial film', *Optics Letters* **22**, 1745–1747 (1997)

[84] K. BUSE, F. HAVERMEYER, L. GLABASNIA, K. SCHLOMP, AND E. KRATZIG, 'Quadratic polarization-optic coefficients of cubic $KTa_{1-x}Nb_xO_3$ crystals', *Optics Communications* **131**, 339–342 (1996)

[85] J. HAUDEN, H. PORTE, AND J. P. GOEDGEBUER, 'Quasi-Polarization-Independent Mach-Zehnder Coherence Modulator Demodulator Integrated in Z-Propagating Lithium-Niobate', *IEEE Journal of Quantum Electronics* **30**, 2325–2331 (1994)

[86] W. L. CHEN, R. S. CHEN, J. H. LEE, AND W. S. WANG, 'Lithium-Niobate Ridge Wave-Guides by Nickel Diffusion and Proton-Exchanged Wet Etching', *IEEE Photonics Technology Letters* **7**, 1318–1320 (1995)

[87] P. DAINESI, L. THEVENAZ, AND P. ROBERT, 'Intensity modulation in two Mach-Zehnder interferometers using plasma dispersion in silicon-on-insulator', *Applied Physics B-Lasers and Optics* **73**, 475–478 (2001)

[88] R. SONG, H. SONG, AND W. H. STEIER, 'Novel Mach-Zehnder Polymer Modulators Using Coplanar Waveguide Electrodes', *Frontiers in Optics* (2005)

[89] R. DEKKER, 'All-optical processes in integrated optical devices using materials with large third-order nonlinearities and gain', *Ph.D. thesis, University of Twente, The Netherlands* (2007)

[90] F. MICHELOTTI, A. DRIESSEN, AND M. BERTOLOTTI, 'Microresonators as building blocks for VLSI photonics', *AIP Conference proceedings* (2003)

[91] C. HERZOG, G. POBERAJ, AND P. GÜNTER, 'Electro-optic behavior of lithium niobate at cryogenic temperatures', *submitted to Optics Communications* (2007)

[92] W. N. LAWLESS, 'Specific-Heats of Para-Electrics, Ferroelectrics, and Anti-ferroelectrics at Low-Temperatures', *Physical Review B* **14**, 134–143 (1976)

[93] R. T. SMITH AND F. S. WELSH, 'Temperature Dependence of Elastic, Piezo-electric, and Dielectric Constants of Lithium Tantalate and Lithium Niobate', *Journal of Applied Physics* **42**, 2219– (1971)

[94] M. VEITHEN AND P. GHOSEZ, 'First-principles study of the dielectric and dynamical properties of lithium niobate', *Physical Review B* **65** (2002)

[95] T. SUZUKI, O. EKNOYAN, AND H. F. TAYLOR, 'Electrooptic Coefficient Measurements in $LiTaO_3$ and $LiNbO_3$ Wave-Guides', *Journal of Lightwave Technology* **11**, 285–289 (1993)

[96] K. CHAH, M. D. FONTANA, M. AILLERIE, P. BOURSON, AND G. MAL-OVICHKO, 'Electro-optic properties in undoped and Cr-doped $LiNbO_3$ crystals', *Applied Physics B-Lasers and Optics* **67**, 65–71 (1998)

[97] J. D. ZOOK, D. CHEN, AND G. N. OTTO, 'Temperature Dependence and Model of Electro-Optic Effect in $LiNbO_3$', *Applied Physics Letters* **11**, 159– (1967)

[98] A. M. GLASS AND M. E. LINES, 'Low-Temperature Behavior of Spontaneous Polarization in $LiNbO_3$ and $LiTaO_3$', *Physical Review B* **13**, 180–191 (1976)

[99] S. VIEIRA, 'Pyroelectric Behavior of $LiNbO_3$ at Low-Temperatures', *Applied Physics Letters* **38**, 472–473 (1981)

[100] S. VIEIRA, 'Primary and Secondary Contributions to Spontaneous Polarization of $LiNbO_3$ Below 50 K', *Physical Review B* **24**, 6694–6697 (1981)

[101] B. VAN ZEGHBROECK, 'Optical data communications between Josephson-junction circuits and room-temperature electronics', *IEEE Trans. Appl. Sup.* **3**, 2881 (1993)

[102] T. TSANG AND V. RADEKA, 'Progress in the Optoelectronic Analog Signal Transfer for High Energy Particle Detectors', *Proc. 2nd Intern. Conf. on Electronics for Future Colliders* (1992)

[103] K. YOSHIDA, K. IKEDA, AND Y. KANDA, '$LiNbO_3$ Optical Modulator with Superconducting Electrodes', *IEICE Transactions on Electronics* **E75c**, 894–899 (1992)

[104] J. MORSE, K. MCCAMMON, C. MCGONAGHY, D. MASQUELIER, H. GAR-RETT, AND M. LOWRY, 'Characterization of lithium niobate electro-optic modulators at cryogenic temperatures', *Proceedings of the SPIE - The International Society for Optical Engineering* **2150**, 283–291 (1994)

[105] C. MCCONAGHY, M. LOWRY, R. A. BECKER, AND B. E. KINCAID, 'The performance of pigtailed annealed proton exchange $LiNbO_3$ modulators at cryogenic temperatures', *IEEE Photonics Technology Letters* **8**, 1480–1482 (1996)

[106] J. S. Browder and S. S. Ballard, 'Thermal-Expansion Data for Eight Optical Materials from 60 K to 300 K', *Applied Optics* **16**, 3214–3217 (1977)

[107] D. Haertle, G. Caimi, A. Haldi, G. Montemezzani, P. Günter, A. A. Grabar, I. M. Stoika, and Y. M. Vysochanskii, 'Electro-optical properties of $Sn_2P_2S_6$', *Optics Communications* **215**, 333–343 (2003)

List of publications

Journal articles

C. HERZOG, S. ARAVAZHI, A. GUARINO, A. SCHNEIDER, G. POBERAJ, AND P. GÜNTER, 'Epitaxial $K_{1-x}Na_xTa_{0.66}Nb_{0.34}O_3$ thin films for optical waveguiding applications', *Journal of the Optical Society of America B* **24**, 829–832 (2007)

C. HERZOG, S. REIDT, G. POBERAJ, AND P. GÜNTER, 'Electro-optic phase modulation in ridge waveguides of epitaxial $K_{0.95}Na_{0.05}Ta_{0.71}Nb_{0.29}O_3$ thin films', *Optics Express* **15**, 7642–7652 (2007)

C. HERZOG, G. POBERAJ, AND P. GÜNTER, 'Electro-optic behavior of lithium niobate at cryogenic temperatures', *submitted to Optics Communications* (2007)

A. GUARINO, M. JAZBINŠEK, C. HERZOG, R. DEGL'INNOCENTI, G. POBERAJ, AND P. GÜNTER, 'Optical waveguides in $Sn_2P_2S_6$ by low fluence MeV He+ ion implantation', *Optics Express* **14**, 2344–2358 (2006)

D. REZZONICO, A. GUARINO, C. HERZOG, M. JAZBINŠEK, AND P. GÜNTER, 'High-finesse laterally coupled organic-inorganic hybrid polymer microring resonators for VLSI photonics', *IEEE Photonics Technology Letters* **18**, 865–867 (2006)

Presentations

C. HERZOG AND A. GUARINO, 'Optical Waveguides in $Sn_2P_2S_6$ Produced by Low Fluence MeV He+ Ion Implantation', *8th European Conference on Applications of Polar Dielectrics (ECAPD'8)*, Metz, F, September 5-8 (2006)

Acknowledgments

The successful completion of this thesis wouldn't have been possible without the noble help and support of all the great people I had the pleasure to work and spend time with for the last five years. You know who you are!

I would like to express my gratitude to

Professor Günter for funding my research.

Germano for being the best co-examiner you can get.

Gorazd for supervising my work and carefully reading all manuscripts.

Andrea for invaluable help and support in so many ways. You're the man.

Steffen for growing the mother of all KNTN films when hope was lost.

Mojca for many helpful discussions and ideas.

Daniele for lots of funny hours and also the dark ones in the lab.

Paolo for political discussions and the graveyard shifts with the server.

Tobi, my loyal breakfast break crossword mate.

Hermann for being Hermann. Accept no substitutes.

Jaroslav for every nanometer of crystal surface flatness.

Reto for the odd chemical brewage and his sunny nature.

Lotti and Liselotte for always being all ears and helpful.

Paul Studerus for his expertise in all things electronic.

Abu for growing the early KNTN flims.

All members of the NLO group for their kindness and friendship.

Biggy ups to my man Arno for everything. What else can I say?

Denise for being there when things were tough.

My parents, who have always supported me.

ACKNOWLEDGMENTS

Curriculum vitae

Christian Herzog, born 10 September 1975 in Freiburg im Breisgau, Germany

1982–1985   Primary school, Freiburg im Breisgau, Germany

1985–1986   Primary school, Tiengen, Germany

1987–1995   Klettgau-Gymnasium, Tiengen, Germany

1995–1996   Civilian service at Arbeiterwohlfahrt in Bad Säckingen, Germany

1996–2001   Study of Physics at the Swiss Federal Institute of Technology Zürich, Switzerland

2001   Graduation with a diploma in experimental physics on "*A single chip micro-nose*" in the group of Prof. Dr. H. Baltes, ETH Zürich, Switzerland

2001–2002   IT consultant for Commerzbank AG in Frankfurt am Main, Germany

2002–2007   Research and teaching assistant in the group of Prof. Dr. P. Günter, ETH Zürich, Switzerland

2007   Ph.D. thesis on "*$K_{1-y}Na_yTa_{1-x}Nb_xO_3$ Thin Films for Integrated Electro-Optics*" in the Nonlinear Optics Laboratory of Prof. Dr. P. Günter at the Institute of Quantum Electronics of ETH Zürich